

**OPTIMIZATION AND EXPERIMENTAL
CHARACTERIZATION OF LEADING
EDGE TUBERCLES IN TRANSONIC
FLOW**

**OPTIMISATION ET
CHARACTÉRISATION
EXPERIMENTALE DE TUBERCULES
SUR LE BORD D'ATTAQUE D'UNE
AILE EN RÉGIME TRANSONIQUE**

A Thesis Submitted to the Division of Graduate Studies
of the Royal Military College of Canada
by

Alexi Levert-Beaulieu, BEng
Second Lieutenant

In Partial Fulfillment of the Requirements for the Degree of
Master of Applied Science in Aeronautical Engineering

May, 2019

© This thesis may be used within the Department of National Defence
but copyright for open publication remains the property of the author.

High Speed, Low Drag.

Acknowledgments

I would like to express my gratitude to my supervisor, Dr. Ruben Perez, for the opportunity to pursue this research and for his continuous guidance and support. I would also like to thank Dr. Asad Asghar, Pierre Bissonnette, Branden Freeman, Charles Sadiq and the technicians of the RMC Mech & Aero machine shop for their continuous support during manufacturing of equipment, and set-up and execution of experiments. Finally, I would like to thank the members of the grad student office for their help, support and friendship.

Abstract

Leveret-Beaulieu, Alexi. M.A.Sc. Royal Military College of Canada, May 2019. *Optimization and Experimental Characterization of Leading Edge Tubercles in Transonic Flow*. Supervised by Ruben E. Perez, B.Eng., M.A.Sc., Ph.D., P.Eng., Associate Professor.

Tubercles are bio-inspired leading edge protuberances used as a passive flow control device that can improve the performance of a wing by altering its flow field. Many investigations have been performed to study the effect of tubercles in low subsonic incompressible flow showing improvements in post-stall performance. Recently, based on the idea that a spanwise variation of pressure may delay the onset of sonic flow and improve the drag divergence Mach number, tubercled wings were investigated in transonic flow. It was found that along the pressure variation there is a change in shockwave formation that may lead to drag improvements. Being able to increase the drag divergence Mach number can lead to a drag decrease for a specific velocity and, for example, for a transport aircraft this implies lower fuel consumption. To date, determination of optimal tubercle shapes in transonic flow has not been performed. In this study, tubercles are optimized using computational fluid dynamics with adjoints providing sensitivity information to a gradient based optimizer. Results from the optimization process and a post-optimal parametric study provided insights into the optimal tubercle shape, flow behavior, and impact on drag performance at low angles of attack. Those numerical findings are further supported by an experimental characterization of the drag force and surface pressure using an indraft transient polysonic wind tunnel. An optimal tubercle shape was found to experimentally improve the drag up to 6% over the same wing with a straight leading edge at very low angles of attack and in transonic flow.

Keywords: bio-inspired, tubercles, aerodynamic shape optimization, transonic flow

Résumé

Levert-Beaulieu, Alexi. M.Sc.A. Collège militaire royal du Canada, Mai 2019.
Optimisation et caractérisation expérimentale de tubercules sur le bord d'attaque d'une aile en régime transsonique. Thèse dirigée par Ruben E. Perez, B.Eng., M.A.Sc., Ph.D., P.Eng., Professeur agrégé.

Les tubercules sont des protubérances sur le bord d'attaque d'une aile. Ils sont un dispositif de contrôle passif d'écoulement qui peuvent améliorer la performance de l'aile. Plusieurs recherches ont été effectuées afin d'étudier l'effet de tubercules dans un écoulement incompressible et subsonique et elles ont démontré une amélioration de la performance après le décrochage. Récemment, basé sur l'idée qu'une variation de pression dans la direction de l'envergure peut créer un délai de l'apparition d'écoulement supersonique, les tubercules ont été étudiés en écoulement transsonique. Il a été trouvé qu'avec la variation de pression il a un changement dans l'apparition de l'onde de choc emmenant une amélioration potentielle de la trainée. Pouvoir augmenter le nombre de Mach où la trainée commence à croître exponentiellement implique une réduction de la trainée à une vitesse spécifique, ce qui pourrait, par exemple, être utile pour réduire la consommation d'essence d'un avion de transport.

Jusqu'à présent, l'optimisation de la forme des tubercules en écoulement transsonique n'a pas encore été effectuée. Dans le cadre de cette étude, les tubercules sont optimisés à l'aide d'analyses numériques de dynamique des fluides et à l'aide de la méthode adjointe. Celle-ci fournit l'analyse du degré de variation à un algorithme d'optimisation à gradient. Les résultats de l'optimisation et d'une analyse paramétrique ont donné des indices à propos de la forme optimale, des nouvelles caractéristiques de l'écoulement et de l'effet sur la performance en terme de trainée à petits angles d'attaque. Les résultats numériques sont ensuite appuyés par des résultats expérimentaux. Ceux-ci incluent des mesures de la force de trainée et de la pression à la surface obtenue dans une soufflerie à suction trisonique. Il a été trouvé que la forme optimale

des tubercules peut améliorer la traînée de 6% à petits angles d'attaque et dans un écoulement transsonique lorsque comparée avec la même aile sans tubercules.

Mots Clefs: bio-inspiré, tubercles, optimization de la forme aérodynamique, écoulement transsonique

Contents

Acknowledgments	iii
Abstract	iv
Résumé	v
List of Tables	ix
List of Figures	x
Nomenclature	xiii
1 Introduction	1
1.1 Motivation and Scope	1
1.2 Objectives	2
1.3 Layout of the Thesis	2
1.4 Contributions	2
2 Literature Review	3
2.1 Background	3
2.2 Experimental Studies	4
2.3 Numerical Studies	6
2.4 Tubercle Applications	8
2.5 Tubercles in Transonic Flow	11
3 Flow Simulation	13
3.1 Baseline Geometries	13
3.2 Flow Conditions	14
3.3 CFD Solver and Setup	16
3.4 Grid and Computational Domain	17
3.4.1 Convergence Study	18

3.5	CFD Validation	19
3.6	Baseline Simulation Results	22
3.7	Initial Parametric Study	27
3.8	Constant NACA 0012 Tubercled Wing	27
4	Optimization	31
4.1	Optimization Problem	31
4.2	Optimization Framework	32
4.2.1	Free Form Deformation Box	32
4.2.2	CFD Analysis	34
4.2.3	Sensitivity Analysis	35
4.2.4	Optimization Algorithm	35
4.3	Optimization Results	36
4.3.1	Optimization Convergence	36
4.3.2	Shape Parametrization	39
4.4	Tubercle Shape Parametric Study	40
4.5	Optimization Result Sensitivity	43
4.6	Flow Analysis of the Optimal Transonic Tubercle Shape	45
4.6.1	Angle of Attack Performance	53
5	Experiments	55
5.1	Methodology	55
5.1.1	Experimental Setup	55
5.1.2	Force Measurements	58
5.1.3	Surface Pressure Measurements	61
5.1.4	Surface Flow Visualization	63
5.2	Experimental Results	63
6	Conclusions and Recommendations	69
6.1	Conclusions	69
6.2	Recommendations for Future Developments	70
	Bibliography	71
	Appendices	77
A	Additional CFD Results	78
A.1	Turbulent Kinetic Energy and Turbulent Viscosity	78
B	Additional Experiments	85
B.1	Compilation of Drag Measurements	85

B.2 Schlieren Visualization 86

List of Tables

3.1	CFD freestream flow conditions.	16
3.2	Mach 0.83 drag count RANS results of the triangular and sinusoidal tubercle wing compared with the straight leading edge.	23
3.3	Mach 0.83 drag count of the triangular tubercle wing with different wavelength and amplitude using a RANS solution.	27
3.4	Mach 0.83 drag count RANS results of two constant t/c triangular tubercle wings compared with the straight leading edge.	28
4.1	Drag count results for the parametric study of the power series. . .	42
4.2	Drag count results for the parametric study of alternative shape functions.	43
4.3	Mach 0.83 drag count results of the power $n = 0.20$ with different wavelength and amplitude.	43
4.4	Mach 0.83 drag count results of the power $n = 0.20$ compared with the baseline and triangular tubercle.	45
4.5	Mach 0.83 aerodynamic performance results at two angles of attack for the power $n = 0.20$ compared with the baseline and triangular tubercle.	54
5.1	Drag count comparison of two tubercled wings to the straight leading edge wing using experiments and CFD.	64

List of Figures

3.1	Baseline wings.	14
3.2	Sinusoidal tubercle wing.	15
3.3	Euler grid.	17
3.4	RANS grid.	18
3.5	Grid convergence studies of the triangular tubercle wing for a Mach number of 0.83 and angle of attack of zero degrees.	19
3.6	Drag convergence of sample simulations of the triangular tubercle wing for a Mach number of 0.83 and angle of attack of zero degrees.	20
3.7	Residuals of sample simulations of the triangular tubercle wing for a Mach number of 0.83 and angle of attack of zero degrees.	20
3.8	Simulated and experimental C_p curves ($Re = 3.0 \times 10^6$) for the straight leading edge wing at two Mach numbers and angle of attack of zero degrees.	21
3.9	Simulated and experimental C_p curves ($Re = 6.6 \times 10^6$) for the straight leading edge wing at Mach 0.83 and angle of attack of zero degrees.	22
3.10	Straight leading edge wing simulated pressure at Mach 0.83.	24
3.11	Triangular tubercle wing simulated pressure at Mach 0.83.	25
3.12	Sinusoidal tubercle wing simulated pressure at Mach 0.83.	25
3.13	C_p curves of the two baseline tubercled wing compared to the straight leading edge in the shock region downstream of the peak.	26
3.14	Constant NACA 0012 tubercled wings.	28
3.15	Variable thickness NACA 0012 tubercled wing simulated pressure at Mach 0.83.	29
3.16	Constant thickness NACA 0012 tubercled wing simulated pressure at Mach 0.83.	30
3.17	Streamlines near the leading edge of the triangular tubercle wing at Mach 0.83.	30

4.1	SU2 aerodynamic shape optimization process.	33
4.2	FFD box defined for the triangular tubercled wing.	34
4.3	Top view of the FFD box defined for the triangular tubercled wing.	34
4.4	Objective function history.	37
4.5	Original triangular tubercles and optimized tubercle shapes of three sample iterations.	38
4.6	Convergence rate history.	38
4.7	Illustration of a power function fitting ($n = 0.75$) on the optimized tubercle shape of iteration 10.	39
4.8	Power $n = 0.75$ tubercles.	40
4.9	Graph of sample power functions applied on tubercles.	41
4.10	Graph of alternative shape functions applied on tubercles.	42
4.11	Planform surface sketch of the recreated wing from an optimization with constant volume constraint.	44
4.12	C_p contours of three wings at Mach 0.83.	46
4.13	C_p curves of three wings at Mach 0.83.	47
4.14	Spanwise friction coefficient of two tubercled wings at Mach 0.83.	49
4.15	C_p curves of the two tubercled wing compared to the baseline in the shock region of the valley.	49
4.16	Mach number contours of three wings at Mach 0.83.	50
4.17	Streamlines in the valley of the power $n = 0.20$ leading edge wing at Mach 0.83.	51
4.18	Mach number contour in front of the leading edge of two tubercled wing at a freestream Mach number of 0.83.	51
4.19	Mach number contour close up of the straight leading edge wing at Mach 0.83.	52
4.20	Mach number contour close up of the power $n = 0.20$ tubercle wing at Mach 0.83.	53
5.1	Indraft transient polysonic wind tunnel schematic.	56
5.2	View of the test section.	57
5.3	Wing fixture for the load cell.	59
5.4	Wing fixture for the load cell with fairing.	59
5.5	Straight leading edge wing pressure tap locations.	62
5.6	Power $n = 0.20$ leading edge wing pressure tap locations in inches.	62
5.7	Experimental C_p curves of the power $n = 0.20$ and straight leading edge wing at Mach 0.825.	65
5.8	Experimental C_p contour of the straight leading edge wing at Mach 0.825.	66

5.9	Experimental C_p contour of the power $n = 0.20$ leading edge wing at Mach 0.825.	66
5.10	Schlieren visualization of the straight leading edge wing at Mach 0.82.	67
5.11	Surface flow visualization of three wings at Mach 0.82.	68
A.1	Turbulent viscosity for the baseline wings at Mach 0.83.	79
A.2	Turbulent viscosity of the power $n = 0.20$ and straight leading edge wing at Mach 0.83.	80
A.3	Turbulent kinetic energy for two wings at Mach 0.83.	81
A.4	Turbulent kinetic energy for the triangular tubercle wing at Mach 0.83.	82
A.5	Turbulent kinetic energy for the sinusoidal tubercle wing at Mach 0.83.	83
B.1	Compilation of drag measurements.	85
B.2	Compilation of drag measurements near a Mach number of 0.81.	86
B.3	Schlieren setup schematic.	87
B.4	Schlieren visualization of the straight leading edge wing at Mach 0.82.	87
B.5	Schlieren visualization of the triangular leading edge wing at Mach 0.82.	88
B.6	Schlieren visualization of an elliptical leading edge wing (with an amplitude of $0.25c$ and wavelength of $0.3c$) at Mach 0.82.	88

Nomenclature

Roman Symbols

A	Amplitude	[m]
a	Speed of sound	[m/s]
AR	Aspect ratio	[-]
b	Span	[m]
c	Chord	[m]
D	Drag force	[N]
f	Objective function	[-]
F_z	Streamwise force	[N]
g	Constraint function	[-]
L	Lift force	[N]
M_∞	Mach number	[-]
n	Exponent of the power series equation	[-]
p_∞	Freestream static pressure	[Pa]
p_s	Surface static pressure	[Pa]
p_{atm}	Atmospheric pressure	[Pa]
$R = 287$	Specific gas constant for dry air	[J/(kg K)]
Ra	Roughness height	[μm]
S	Planform area	[m ²]

T	Room temperature.....[K]
t	Thickness.....[m]
t/c	Thickness to chord ratio [-]
U_∞	Freestream velocity [m/s]
x	Variable defining a direction, can also be a design variable [m]
y	Variable defining a direction, can also be a design variable [m]
z	Variable defining a direction, can also be a design variable [m]

Greek Symbols

$\gamma = 1.4$	Ratio of specific heats [-]
λ	Wavelength.....[m]
μ_t	Turbulent viscosity..... [kg/(m s)]
ρ	Freestream dry air density..... [kg/m ³]
$\tau_{w,y}$	Spanwise wall shear stress [Pa]

Dimensionless Groups

$C_D = \frac{D}{0.5\rho U_\infty^2 S}$	Drag coefficient
$C_L = \frac{L}{0.5\rho U_\infty^2 S}$	Lift coefficient
$C_p = \frac{p_s - p_\infty}{0.5\rho U_\infty^2}$	Pressure coefficient
$C_{f,y} = \frac{\tau_{w,y}}{0.5\rho U_\infty^2 S}$	Spanwise Friction Coefficient

Roman Subscripts

lb	Lower bound
ub	Upper bound

1 Introduction

1.1 Motivation and Scope

Drag reduction has important ramifications and, for example, with transport aircraft can positively influence performance, cost and the environmental impact because of possible improvements in weight and fuel consumption [1, 2]. A reduction of one drag count (where one drag count is equal to a drag coefficient, C_D , of 0.0001) can translate to an increase of around 200 lbs in payload for a subsonic civil transport aircraft [1, 3]. In the transonic regime, as the speed increases past the critical Mach number, an airfoil will experience a substantial rise in drag due to the presence of shockwaves, which is a type of drag named wave drag. This drag rise phenomenon is called drag divergence and its avoidance is the reason for the cruise Mach 0.8 plateau associated with most transport aircraft [2]. Thus, an increase in the drag divergence Mach number, defined as the Mach number at which $dC_D/dM = 0.10$ [4] and represents the point when drag divergence becomes significant, is desirable for the considerable decrease in drag for the same speed. Methods used to reduce wave drag include sweep, supercritical airfoils, local porosity and local wall deformations such as bumps or Küchemann carrots (a detailed description of those methods can be found in Bushnell [2] and Küchemann [5]). An alternative for wave drag reduction has been explored within the last two years with a modification to the leading edge shape of the wing with the use of tubercles, which are bio-inspired leading edge protuberances. Their use in transonic flow was found to indicate a potential in drag improvement because of a reduction in shockwave strength [6–10]. The use of those types of flow control device can help in reducing the complexity and the structural weight of an aircraft by the use of a smaller wing, a reduced sweep, a thicker wing, or smaller and simpler high lift systems [1]. Although the addition of tubercles for the reduction of wave drag has been studied in the past, the shape of the tubercle itself was never designed or optimized with regards to transonic flow conditions and this became the scope of this thesis.

1.2 Objectives

This study aims to optimize the shape of the tubercles in transonic flow, and more specifically:

- Simulate using computational fluid dynamics (CFD) the tubercled wings from previous work to provide confidence in the simulation as well as benchmark data for future comparisons. This simulation also provides the groundwork for the following objective.
- Optimize the tubercles in order to find a new shape that improves the drag characteristics of an NACA 0012 wing at an angle of attack of zero degrees.
- Support the findings of the optimization and simulations with wind tunnel experiments.

1.3 Layout of the Thesis

The remainder of this thesis is organized into four chapters. Chapter 2 presents a literature review of previous work done in the field of tubercles applied on the leading edge of wings. This includes the aerodynamic effects of tubercles in low subsonic incompressible flow, select examples of application of tubercles, and all current research regarding the impact of tubercles in transonic flow. Chapter 3 describes the necessary background in terms of simulation tools which is then followed by the results of the baseline geometries' simulations. With this starting point and a simulation model, it was possible to start optimizing. The optimization process and results are the focus of Chapter 4. Experimental testing was then done in order to support the numerical findings of the simulations and optimization. The experimental setup and results are detailed in Chapter 5. Chapter 6 provides concluding remarks and recommendations for further research on this topic.

1.4 Contributions

- An approach for the optimization of the shape of leading edge tubercles.
- The development of a parameterized tubercle shape to reduce drag when added to the leading edge of a wing in the transonic regime.
- A better understanding of the drag sensitivity with regards to modifications in tubercle shape and other tubercle characteristics such as wavelength and amplitude.
- Insights into desirable tubercle related flow features for drag reduction.

2 Literature Review

Leading edge protuberances, also called tubercles, have become a fast growing research area. The effect of leading edge tubercles on aerodynamic performance, possible explanations of the mechanisms through which tubercles alter the flow characteristics and many potential applications have been explored. This chapter presents previous studies pertaining to the subject of tubercles starting with the origin of tubercle research followed by select examples from the experimental and numerical campaign, and various topics where tubercles have been applied. All of the current research on the use of tubercles in transonic flow is also covered.

2.1 Background

Flow control can be an important factor in the movement of aquatic animals as their mobility, which includes turning performance, is dictated by the hydrodynamic characteristics of their bodies [11]. Recently, there has been a growing interest in tubercles as a passive flow control device. Tubercles are bioinspired rounded, leading edge protuberances that alter the flow field around a wing and can enhance its performance [12, 13]. They were initially bioinspired from the leading edge of flippers of the humpback whale. This whale is described as the most acrobatic of cetaceans [14] and was observed to have a high degree of maneuverability during feeding [13, 15–17]. In fact, with the use of its flippers, the humpback whale is able to execute very sharp turns at high swimming speeds (greater than 4 knots [2m/s]) [15]. Knowing this travel speed and the average chord length of the flipper the Reynolds number was estimated to be around 10^6 [11, 12]. Although not in water, this is in a possible Reynolds number range for general aviation and many small Unmanned Air Vehicles (UAV), and tubercles are studied to this day on the promise of improved maneuverability, and improved aerodynamic and hydrodynamic performance.

Fish and Battle [13] were the first to measure and evaluate the morphology of the flipper of the humpback whale and most of the subsequent tubercle research was based on their measurements. They characterized the design of the whale flippers and noticed the presence of tubercles, recorded their positions and noted that the flipper section is symmetrical and similar in design to the NACA 63₄–021 airfoil. They also recorded the variation of chord and thickness and noted that the flipper planform was elliptical, tapered and had a 19 degree sweep relative to the longitudinal axis. They also theorized that tubercles may improve hydrodynamic performance as a passive method of flow control. More precisely, they discussed the possibility of stall delay, increased lift generation and a decrease of drag stemming from the presence of vortices originating from the tubercles. Flow visualization of a model wing section demonstrated the presence of vortices but their effect on performance was not characterized in their study. From this seminal work, many researchers started to investigate the effect of the presence of leading edge tubercles on wings in low subsonic incompressible flow.

2.2 Experimental Studies

Miklosovic *et al.* [11] measured the aerodynamic performance of a scaled model of an idealized humpback whale flipper in a wind tunnel and compared the performance variations of the flipper with and without tubercles. The models were based on an NACA 0020 airfoil and tested at a maximum Mach number of 0.2 with Reynolds numbers from 5.05×10^5 to 5.20×10^5 and angles of attack from -2 to +20 degrees. They found that leading edge tubercles delay the stall angle by about 40%, increase the maximum lift by 6%, and decrease drag beyond an angle of attack of 12 degrees by as much as 32%. They were the first to observe that tubercles act in a manner similar to vortex generators as they may cause a momentum exchange with the boundary layer, which helps to keep flow attached.

Johari *et al.* [18] experimentally measured the aerodynamic forces of airfoils with eight different leading edge tubercle geometries in a water tunnel. Airfoils with different combinations of amplitudes and wavelengths for the sinusoidal tubercles were all compared to a baseline 63₄–021 airfoil. The geometry of the airfoil and tubercles were chosen based on the morphology of the humpback whale flipper. They found that airfoils with tubercles enhanced the post-stall performance by providing a post-stall lift of up to 50% higher than the baseline without drag penalty at a Reynolds number of 1.83×10^5 . The pre-stall

drag was found to be higher for the modified airfoils. By comparing different combinations of wavelengths and amplitudes, they found that the wavelength had little effect on forces and moment coefficient although a smaller wavelength was found to perform slightly better, and that a change of amplitude had a substantial impact. A larger amplitude lowers the maximum lift coefficient while smoothing the lift curve near stall. Flow visualization with tufts revealed that the flow remains attached well past the stall angle of the baseline airfoil and that flow separation originates in the valleys of modified airfoils. The investigation of the flowfield and the mechanisms for the observed tuft flow patterns was not addressed.

Miklosovic *et al.* [19] further explored the effects of tubercles on finite wings with models based on a NACA 0020 profile. The experiments were completed in a wind tunnel at Reynolds numbers between 2.74×10^5 and 2.77×10^5 and a Mach number of 0.13 for the square wings, and at Reynolds numbers between 5.34×10^5 and 6.31×10^5 and a Mach number of 0.21 for the whale fin models. They observed that performance improvements for the square wing occur only beyond stall where tubercles increased lift by as much as 48% and decreased drag by up to 6%, but before stall the maximum lift coefficient is reduced and drag largely increased. For the whale fin model, because of the different planform shape, the effects of tubercles were favorable on a larger range of angles of attack with an observed delayed stall after a higher maximal lift coefficient and decreased drag when comparing to the wing without tubercles. This study indicates that tubercles may benefit from both the planform shape and the higher Reynolds number.

Hansen *et al.* [20] carried out wind tunnel experiments at a Reynolds number around 1.2×10^5 to determine the influence of sinusoidal tubercles on the performance of two different NACA airfoils, a NACA 65-021 and a NACA 0021, with various combinations of amplitudes and wavelengths. Hydrogen bubble visualization was also done in a water tunnel with Reynolds numbers up to 5250. They found that, for both airfoils, reducing the amplitude leads to a higher maximum lift and larger stall angle but having a large amplitude leads to better post-stall performance. Reducing the wavelength leads to better performance, but at a certain point a reduction of wavelength has a negative impact, which points towards the existence of an optimal wavelength. With the flow visualization they confirmed the greater degree of flow attachment at the peak, which points towards the presence of streamwise vortices. They also observed an increase in momentum exchange with smaller wavelengths which helped to keep the flow attached. The presence of tubercles is found to be

favorable in the pre-stall and post-stall regime for the NACA 65-021 airfoil. Whereas for the NACA 0021 airfoil performance is increased post-stall but decreased pre-stall. For both airfoils the stall is much more gradual, the post-stall lift is greater, the post-stall drag is lower, and there is minimal difference in drag at low angles of attack. They were not able to explain the mechanism by which the flow characteristics alter aerodynamic performance.

2.3 Numerical Studies

Watts and Fish [21] developed a three-dimensional panel method simulation with an inviscid approach and used it to compare the forces acting on a NACA 63₄ – 021 square wing ($AR = 2.04$) with and without sinusoidally shaped tubercles at an angle of attack of 10 degrees, and a large Reynolds number. They reported a 4.8% increase in lift, a 10.9% reduction in induced drag, a 17.6% increase in lift to drag ratio, and a possibility of stall delay. They suggested studying possible performance improvement by modifying the tubercle shape and spacing, and to experimentally study the effect of tubercles past stall to evaluate the potential gains in that regime.

Pedro and Kobayashi [22] were the first to simulate wings with tubercles with CFD. They used a detached eddy simulation (DES) formulation to solve turbulent flow with the objective of improving the understanding of the mechanisms behind the aerodynamic performance improvements of wings with tubercles. They simulated the two wings inspired by the humpback whale flipper of the wind-tunnel experiments of Miklosovic *et al.* [11]. The analysis was done at a Reynolds number of 5×10^5 and at select angles of attack including at flow separation (from 12 to 18 degrees). Their results show a very good agreement with experiments and the main findings of the analysis are that the Reynolds number influences the type of separation and that the increased aerodynamic performance is due to the presence of streamwise vortices that originates from the tubercles. These vortices give momentum to the boundary layer which helps in delaying the trailing edge separation, and also help by confining the leading edge separation to the wing tip.

Van Nierop *et al.* [23] developed an analytical aerodynamic model to explain the increase of stall angles of wings with leading edge tubercles. The model predicts that as the amplitude is increased, the lift slope decreases and that stall delay is insensitive to the wavelength. They argued that since the thickness is fairly constant but the chord length varies from the peak to the valley,

the pressure gradient is higher at the valley and thus separation initiates at that location. This correlates with the experimental observation of Johari *et al.* [18]. They also discussed a more gradual stall and higher overall stall angle with the model. They hypothesized that a factor that contributes to stall delay is a nonuniform downwash that is found to be larger at the peak when compared to the valley, which leads to a decrease of the effective angle of attack. The authors suggest as future work to address the differences in performance improvements between the finite wing of Miklosovic *et al.* [11] and all other studies using infinite wings, and address the role of leading edge vortices and wing tip effects.

Weber *et al.* [24] used CFD to investigate the effect of tubercles on the idealized humpback whale flipper of Miklosovic *et al.* [19]. Two solvers, STAR-CCM+ and SolidWorks Flow Simulation, were used in their study to solve Reynolds averaged Navier-Stokes (RANS) equation closed with select turbulence models including Spalart Allmaras (SA), $k - \omega$ and $k - \epsilon$. Lift and drag predictions were found to be accurate in the pre-stall region with a maximum error on lift of 6.6% between both solvers, although predictions in the stall region was found to be considerably less accurate than the results obtained in Pedro and Kobayashi [22] with DES. The Solidworks Flow Simulation solver (using RANS with $k - \epsilon$) gave results that were in better agreement with the experiments in post-stall than STAR-CCM+ (using RANS and $k - \omega$ in the post-stall region). With flow visualizations they noted that the tubercled flipper tended to stall from the region of the tubercle valleys, has a pressure differential between the peak and the valley, and is able to obtain a larger lift coefficient post-stall due to regions of the flow remaining attached along the flipper span. Even if they did not include other turbulence models, such as the Shear Stress Transport (SST) model, their study brings to light some limitations of CFD solvers that implement the RANS equations when there are complex flow effects from low Reynolds number and detached flows. RANS can be useful to support experimental results but its use for predictions must be done with care as there is a risk of neglecting phenomena that have an impact on lift and drag.

The way that tubercles affect the aerodynamic performance of a wing was found, experimentally and numerically, to depend on the amplitude and wavelength of the tubercles (usually sinusoidal in shape), the Reynolds number, the airfoil shape and the planform shape. However, nothing conclusive was found in terms of trends because of the large impact of many variables related to, for example, the geometry and the flow conditions. Lohry *et al.* [25]

applied a multi-objective genetic algorithm to the optimization problem of tubercles on an infinite NACA 0020 wing in unsteady RANS simulations to have an automatic exploration of the design space. Their objective function was the improvement of lift near the maximum lift angle and at a post-stall angle (14 and 20 degrees respectively). They optimized lift performance at a Mach number of 0.1 and a Reynolds number of 5×10^5 . They found strong evidence that a leading edge variation will not improve the maximum lift in the infinite wing case. In post-stall, the tubercles had clear improvements with large amplitudes and a high tubercle frequency. They did not find any design that maintains or improves the maximum lift coefficient and improves post-stall lift while also maintaining the spanwise-average shape of the NACA 0020 profile. The authors suggested that further research is required for the finite wing case, and with a reduction of the complexity of the design space.

2.4 Tubercle Applications

The favorable aerodynamic impact from the unique flow control mechanism of tubercles made it desirable for many studies to look further into more practical applications. There are numerous attempts to study tubercles in relation to a specific purpose and this section presents some examples.

The noise coming from the interaction of an airfoil (from, for example, wind turbines, aircrafts and propellers) and flow turbulence is called broadband noise and it covers a large section of the audible range. The characteristic high pitched noise associated with the circulation of a fluid over those airfoils is within the broadband noise range and is called tonal noise. [26] Hansen *et al.* [27] conducted a study on the NACA 0021 in order to experimentally determine the effect of tubercles on these types of noise. The addition of tubercles was found to eliminate tonal noise and considerably reduce broadband noise. The authors found that the tubercle amplitude and wavelength affected this change and they concluded that the larger amplitudes and smaller wavelengths were the most effective configurations to eliminate tonal noise. In another study, Asghar *et al.* [28] tested tubercled propellers to quantify their acoustic characteristics and they found a clear indication of potential acoustic emissions reduction with no deterioration in performance. These findings could have important implications with regards to improvements in the noise signature of, for example, small commercial and military UAVs [28].

The dynamic stall phenomenon is usually associated with rotating blades, such as wind turbines, helicopters, propellers and is caused when a vortex, created by the reverse flow of the rotating wing, moves from the leading edge to the trailing edge and then off the wing's surface [26]. The lift and pitching moment then suddenly decrease resulting in stall. When the blades operate beyond the critical stall angle of attack of the wing, there is time dependent flow separation and large load hysteresis that leads to fatigue [26]. The implementation of tubercles on rotating wings was found to reduce dynamic stall. For example, Borg [29] experimentally studied the effect of tubercles on dynamic stall with an NACA 0021 airfoil at $Re = 1.3 \times 10^5$. There was a hysteresis reduction of 39% and an increase in the maximum lift coefficient of 26%. He obtained best results from tubercles with low amplitudes and low wavelengths. Cai *et al.* [30] also contributed to the same research area with the numerical study of a NACA 63₄ - 021 airfoil at $Re = 2 \times 10^5$. They found that tubercles can improve the consistency of flow during dynamic stall conditions within a particular range of angles of attack, avoiding the delay of separation and reattachment. This causes a more gentle hysteresis. Although not directly investigating the subject of dynamic stall, Asghar *et al.* [31] applied different combinations of tubercle configurations on small scale aircraft propellers and found up to 6% improvement in propeller efficiency. All these studies point towards viable potential application of tubercles on rotating blades but more research is needed to establish which tubercle configurations improve performance in a particular scenario.

Gupta *et al.* [32] performed a CFD study on three different designs of NACA 4412 blades for a horizontal wind turbine. One of the designs included leading edge tubercles. They found that the blade with tubercles produced almost less than a quarter of the power of the baseline but demonstrated more stability of the flow over the blade. They suspected that, because of this stability, the blade has potential at higher wind speeds. They also suggested that having a thicker airfoil may improve the results. Huang *et al.* [33] experimentally studied the effect of tubercles on a variable speed horizontal axis wind turbine with the SD8000 low Reynolds number airfoil. Their results show that the model with smaller amplitude of tubercles performed better than the baseline in the stall region. Abate and Mavris [34] simulated with CFD the effect of leading edge tubercles on the power produced and Annual Energy Production (AEP) of a National Renewable Energy Laboratory (NREL) Phase VI wind turbine. Their results show that the energy production is improved for the blades with low amplitude and high wavelength tubercles as long as the mean value of the wind speed was above the design point. Note that their simu-

lations were performed with RANS and the SST turbulence model. During their validation, they showed good agreement with experiments before flow separation. As the stall region grew, the simulations had difficulty predicting the pressure distributions, although in deep stall the prediction started to be reasonably accurate again. Wang and Zhuang [35] conducted a numerical study on a vertical-axis wind turbine for which tubercles were implemented on the leading edge of NACA 0018 rotating blades. They found that the power coefficient improved by about 18.7% for a tip-speed ratio of 2. Dynamic stall is also observed to be significantly reduced. On the other hand, Bai *et al.* [36] found using CFD that the thrust of a vertical axis wind turbine with NACA 0015 blades with tubercles are lower than the baseline, and they reported that it is because of the interaction of the vortices generated by the tubercles. It can be said in conclusion that most of the recent research of tubercles and wind turbines are numerical and the findings are inconclusive.

Tubercles were also investigated in relation to several marine applications. Weber *et al.* [37] implemented tubercles on marine rudders and conducted water tunnel experiments for Reynolds number between 2×10^5 and 8.6×10^5 . They presented that tubercles accelerate cavitation, that tubercles can affect the location of the onset of cavitation (appearing first in the valleys), and that for high angles of attack (over 22 degrees), the lift increased. Ibrahim and New [38] numerically investigated the effect of tubercles on a marine propeller. They reported an improvement of 1.5% in thrust at low advance ratios (below 0.55) which also results in a 6% increase in torque and a lower efficiency than the baseline. They concluded that the difference is very small most likely because the tested angles of attack were too small to have flow separation, where the tubercles would be most beneficial. Shi *et al.* [39] applied tubercles to a tidal turbine blade and experimentally confirmed performance improvement because of the tendency of the flow to stay attached and the reduction of the three dimensional effects which leads to an increase in efficiency, torque and thrust. The same research group also investigated the tidal turbine blades using CFD in order to improve the tubercle designs and compromise between the higher post-stall lift and lower maximum lift of wings with tubercles. Their simulations were done in steady state RANS with the SST turbulence model. They described that the simulations correlate well with experiments showing that a properly defined RANS simulations can be an option for the simulation of wings with tubercles [40].

2.5 Tubercles in Transonic Flow

All the above studies only involved low speed flows, low Reynolds numbers, and were concerned with pre to post-stall performance. The idea of applying tubercles in transonic flow, which typically involves wings at low angles of attack and nowhere near stall, was first introduced by Bolzon *et al.* [41]. They theorized that since the pressure over the surface of a tubercled wing fluctuates with regions of lower and higher minimum pressure, the first appearance of sonic flow may be extended and delay the sonic flow of the whole wing. Thus, the addition of tubercles may result in an increase in the drag divergence Mach number. To explore this theory, Asghar *et al.* [6, 7] experimentally investigated the effect of tubercled leading edge wings in transonic flow to reduce wave drag near drag-divergence. They did schlieren flow visualization, surface pressure measurements and surface flow visualization in a transonic wind tunnel with two NACA 0012 wings at zero angle of attack, one with a straight leading edge and the other one with the triangular tubercled leading edge. Shockwave strength reduction and aft displacement was observed with schlieren visualization. They attributed this improvement to the periodic pressure differential between the streamwise flow of the peak and valley of the tubercles. The weaker strength and aft displacement indicates an improvement in the divergent Mach number but it was not quantified in that experiment. Additional pressure measurements showed that there is a pressure differential between the peak and the valley of the tubercle [7]. This differential causes the streamwise flow to have a span-wise component in which the flow can expand further. This expansion explains the downstream migration of the shock wave as it takes more time to equalize the pressure and merge the shock waves to one 2D wave [7]. To try to elucidate the flow features of the tubercled wing, Perez and Asghar [8] undertook some flow simulations in the transonic regime using RANS. The results show agreement with their experiments and consistently presented spanwise pressure variations that led to changes in shock formation, boundary layer interactions and wake.

Studies done by Filho *et al.* [9] numerically investigated with RANS the effect of sinusoidal leading edge tubercles on an NACA 0012 infinite wing at a Mach number of 0.8. They found that the presence of tubercles can increase the aerodynamic efficiency up to 11.2% and decrease the drag by 7.9 drag counts. Sepetauskas *et al.* [10], from the same research group, extended the study by experimentally investigating the impact of sinusoidal tubercles at a Mach number of 0.6 and 0.7 and angles of attack of zero, two and four degrees. They observed a pressure differential between the peak and the valley and a

suppression of a shockwave with the presence of tubercles when the wing was at an angle of attack and at Mach 0.7.

A feature that was not explored in the previous studies of tubercles in transonic flow is that the designed shape was not optimized for the tested flow conditions. This study aims to find an optimum shape for the tubercles starting with the wing of the study by Asghar *et al.* [6,7] and Perez and Asghar [8].

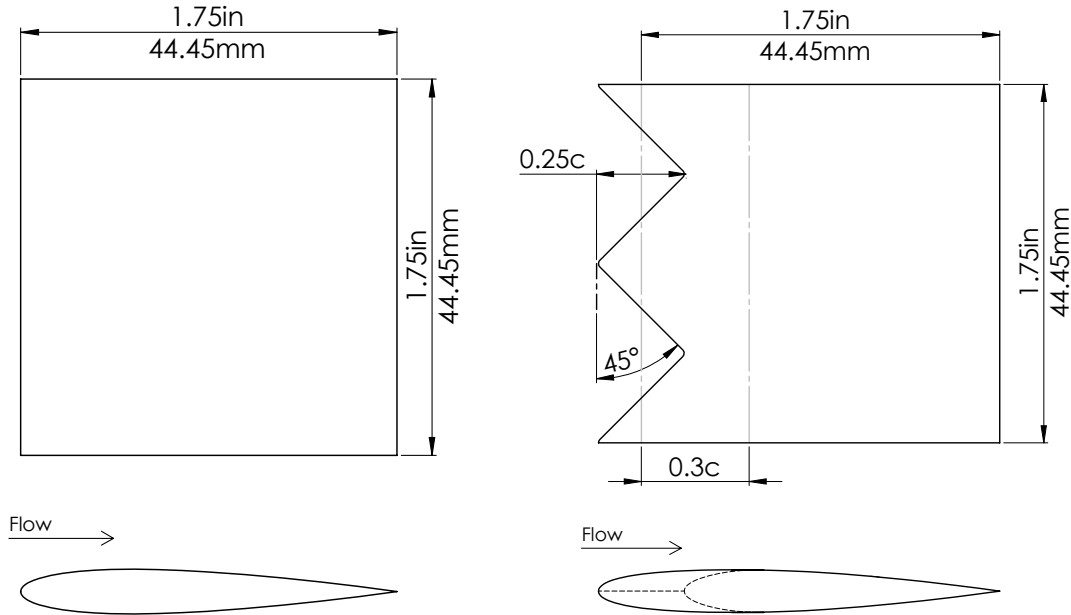
3 Flow Simulation

Prior to the aerodynamic shape optimization, confidence in simulating tubercles in transonic flow has to be established and two CFD solvers were investigated. This chapter presents the baseline geometries, the CFD method and set-up, and the baseline CFD results.

3.1 Baseline Geometries

The baseline wings are taken from the study of Asghar *et al.* [6, 7] and are shown in Figures 3.1a and 3.1b. The airfoil NACA 0012 was also selected for this study because it is a well known airfoil often used in transonic speeds with a large database of available experimental data. A straight leading edge wing based on this airfoil was used as a point of reference to account for the drag improvement of tubercled wings. The span and average chord of the wings were driven by the dimensions of the test section of the Royal Military College of Canada (RMC) transonic wind tunnel in order to directly compare simulation results to experimental data.

For the tubercled geometry, the mean chord matches the one of the straight leading edge wing and the geometry is made to smoothly merge with the reference airfoil shape at 20% of the chord. Note that in order to be able to compare the aerodynamic effect of changing the leading edge shape with tubercles, it was established that the same mean chord, the maximum thickness and mean chordwise position of the maximum thickness is required. As only the leading edge area is modified, the tubercles merge before maximum thickness which is at 30% of the chord for a NACA 0012 airfoil. It was decided to limit the amplitude of the tubercle by merging before maximum thickness in order to have the aft part of the airfoil the same as the straight leading edge wing. The aft part of the wing was kept the same in order to keep a structural integrity which may help with regards to the integration of tuber-



(a) Straight leading edge NACA 0012 wing [6]. (b) Triangular tubercle wing [6].

Figure 3.1: Baseline wings.

cles for potential future practical applications. In terms of shape, the size of the tubercle was originally made to be very large in order to help experimentally visualize differences between the wings, and a small fillet of a radius of 0.025 in (0.635 mm) was added at the corner of the peak and the valley for a more realistic wing in terms of manufacture. A second tubercle shape that is often used in literature, the sine wave leading edge tubercle geometry, was also simulated. Its geometry is shown in Figure 3.2. The only change from the triangular tubercle design is the change in tubercle shape as the amplitude and wavelength was kept the same. The three wings were then simulated with CFD in order to establish their performance and investigate their flow features.

3.2 Flow Conditions

In order to set up the simulations, the flow conditions had to be selected. A summary of the flow conditions used for all the simulations is shown in

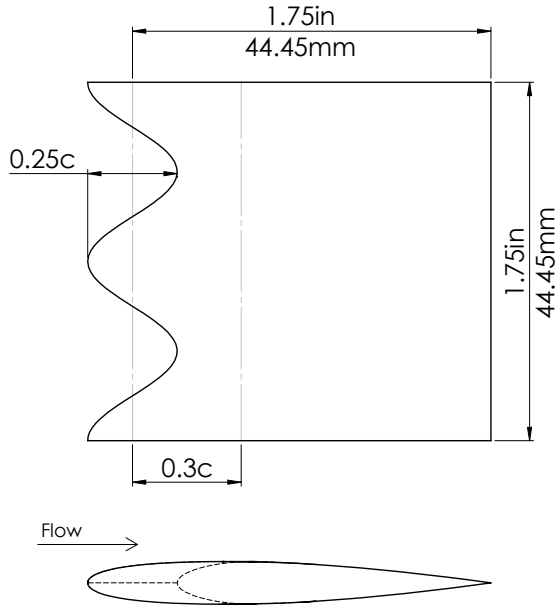


Figure 3.2: Sinusoidal tubercle wing.

Table 3.1. The flow properties were chosen to be at standard sea level (SSL) conditions, which are similar conditions to those of experiments done at the RMC transonic wind tunnel. The angle of attack of the wing was kept at zero degrees as a starting point to gather fundamental knowledge and due to the experimental test section being set up for that angle. This angle was also chosen as it is applicable in practice. For example, all aircraft have a design point (typically at cruise) where drag is minimized and the angle of attack is zero degrees [42]. The simulations were done at a Mach number of 0.83, a velocity near the maximum flow speed achievable in the experimental test section and well into the drag divergence as the drag divergence Mach number of a NACA 0012 wing is between 0.76 and 0.78 [43]. This speed was selected in order to have a high sensitivity to changes in tubercle shape and the differences between wings in terms of flow features may be more evident. Note that the simulated velocity can be easily modified once the CFD framework is established.

Table 3.1: CFD freestream flow conditions.

Flow property	Value	Unit
Pressure	101.325	kPa
Density	1.225	kg/m ³
Dynamic viscosity	1.789×10^{-5}	kg/(m s)
Mach number	0.83	
Reynolds number	8.58×10^5	

3.3 CFD Solver and Setup

The simulations were performed using SU2, which is an open source collection of software tools used to solve problems described by Partial Differential Equations (PDE), and is designed for CFD [44]. It has the capacity of solving Euler, RANS and hybrid RANS-LES equations. The software suite is also able to solve PDE constrained optimization problems, including aerodynamic shape optimization. The SU2 optimal shape design script is built to automate the optimization process which includes functional and gradient computation, the ability to analyze performance, mesh deformation, and an optimization algorithm [44].

The two CFD solvers, compressible Euler and RANS, were considered for the simulations. Euler is a more time efficient simulation that disregards viscosity while RANS solves the Navier-Stokes equation by averaging the solution in time and closing the equations with a turbulence model. RANS is also capable of modeling the boundary layer and shock wave boundary layer interaction (SWBLI) which is important to consider in transonic flow at drag divergence. For this study the RANS equations were closed with Menter’s SST $k-\omega$ turbulence model [45]. The SST model is a two equation turbulence model that can be more accurate than the other available turbulence models in SU2 (which includes the one equation SA model with and without corrections) and requires more computational resources. SST was used because it is more appropriate for compressible flows with strong adverse pressure gradients and flow separation [46, 47]. For both Euler and RANS, Roe’s approximate Riemann solver is used for the spacial discretization [48]. Roe is an upwind solver with high accuracy for boundary layers and a good resolution of shocks [46, 49]. All the simulations were performed in parallel with Message Passing Interface (MPI) on a computer cluster with 40, 2.67 GHz cores.

3.4 Grid and Computational Domain

Unstructured meshes built with tetrahedral cells were generated using the commercial software PointwiseTM. The unstructured type mesh was used to simplify meshing of the wing with tubercles and the same mesh with the same sizing was used to compare between the different wings to eliminate the discretization as a variable in the variation of performance. An example of the Euler mesh is shown in Figure 3.3, and an example of the RANS mesh is shown in Figure 3.4. For a wing with a span of 1.75 in (44.45 mm), the Euler mesh contains 1 million cells and the RANS mesh 7 million cells. Note that the RANS mesh has a region of high density cells as far as 3 chords from the wing in order to precisely analyze the flow near the shockwave. The sizing of the first layer of the modeled boundary layer with RANS meshes were made in order to have a $y^+ \approx 1$ and the boundary layer thickness determined the height of the anisotropic tetrahedral extrusion. With regards to the computational domain, in all the cases, the far field is located at 25 chords from the wing to ensure that the flow interacting with the wing is not affected by the far field. In order to simulate an infinite wing a symmetry boundary condition was imposed at the sides of the wing. For the calculation of aerodynamic forces, a solver dependent wall boundary condition was applied on the surface mesh of the wing.

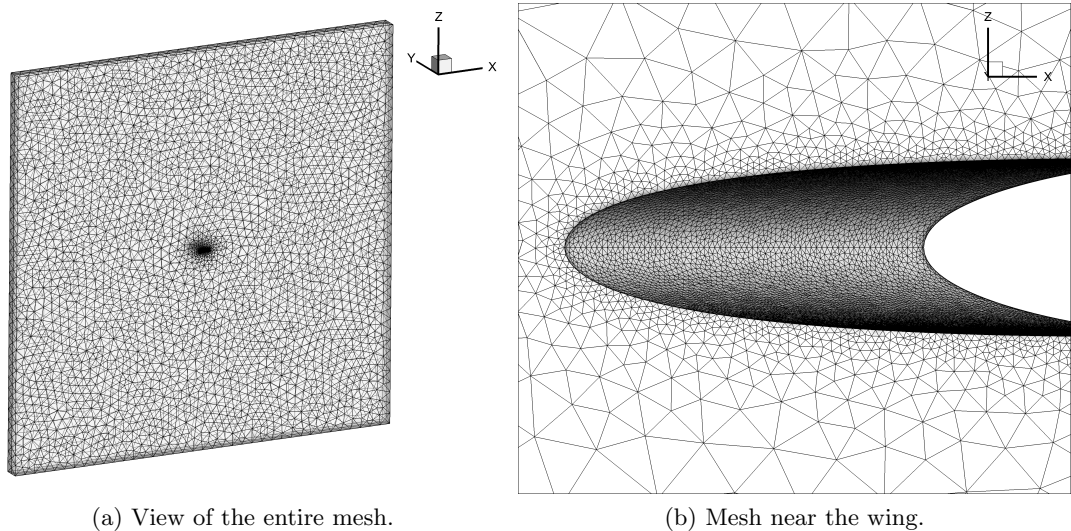
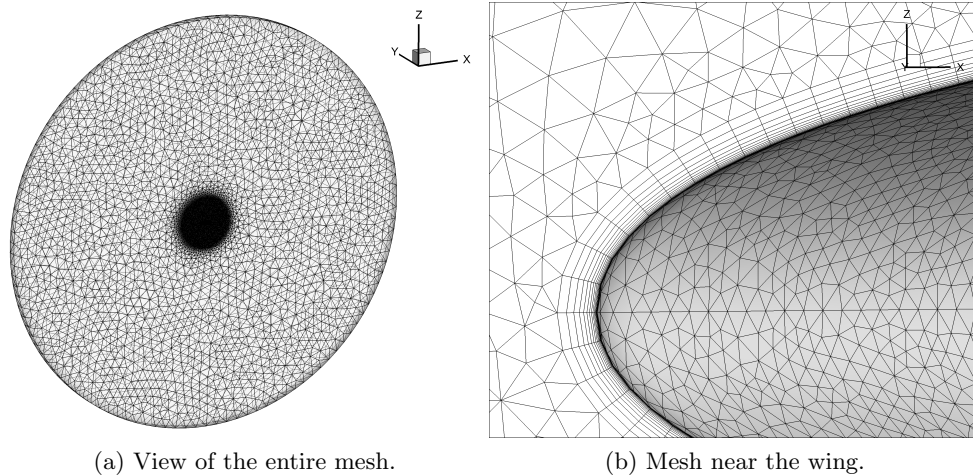


Figure 3.3: Euler grid.



(a) View of the entire mesh.

(b) Mesh near the wing.

Figure 3.4: RANS grid.

3.4.1 Convergence Study

In order to select the number of cells, a convergence study on the triangular tubercle wing was performed in both Euler and RANS. The triangular tubercle wing was used for the convergence study because its simulation involves additional flow characteristics when compared to the 2D flow of the straight leading edge wing. If the mesh of the triangular tubercle converged, the mesh of other wings should be converged as well. Drag counts as a function of the number of cells for both cases are presented in Figure 3.5. A mesh of at least 1 million cells and 4 million cells was judged as sufficiently precise for the Euler and RANS analyses, respectively. Using Euler, drag varies up to 5 drag counts after 1 million cells, and in RANS, the drag varies less than 1 drag count after 4 million cells. There is an indication that the Euler simulation has some difficulty to accurately model the shockwave because the discretization of the geometry has a larger impact on the solution. This is shown with the Euler convergence study as it does not converge to a single value as smoothly as the RANS simulation. The mesh that was used for the RANS simulations was on the order of 7 million cells for an increased precision of the modeling of the surface to account for a potential increase in leading edge curvature during optimization, and the additional computational time was considered as acceptable.

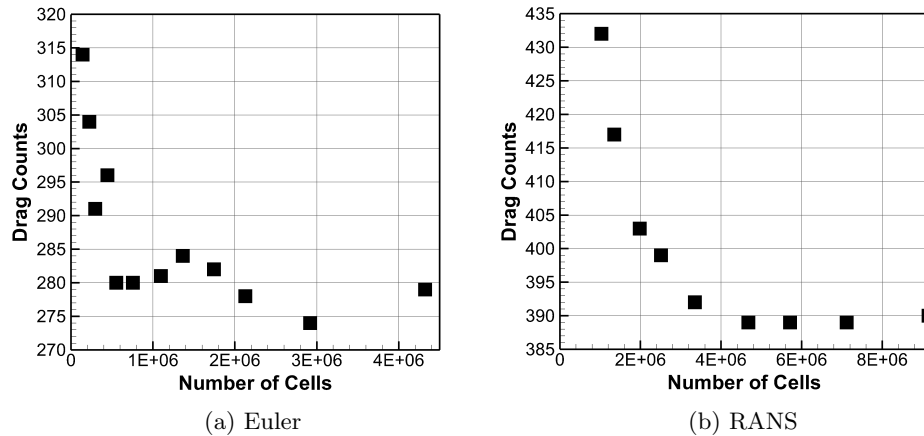


Figure 3.5: Grid convergence studies of the triangular tubercle wing for a Mach number of 0.83 and angle of attack of zero degrees.

Convergence of the results of one RANS simulation was obtained by letting the simulation run for at least 5 000 iterations, with a Courant-Friedrichs-Lewy (CFL) number of 10 (the number defining the time step), which is the number of iterations where all residuals converge. For one Euler simulation, convergence of the simulation was obtained by letting the simulation run for 2 000 iterations with an adaptive CFL number starting with 5. The convergence of the drag coefficient and the residuals are shown for both Euler and RANS in Figures 3.6 and 3.7. Note that the discontinuous behavior of the Euler residuals is due to the adaptive CFL, and with either an adaptive or a constant CFL the solution converges to the same values.

3.5 CFD Validation

In order to verify the validity of the simulations, data obtained from static pressure measurements at three different Mach numbers for the NACA 0012 straight leading edge wing, found in two NASA articles [50,51], was compared to the simulation results. Note that the Reynolds numbers of the literature are larger than the one of this research (the experimental data was taken at $Re = 3.0 \times 10^6$ or $Re = 6.6 \times 10^6$ and they were the lowest ones found in literature for pressure measurements). The comparison can be seen in the pressure coefficient curves of Figure 3.8 and 3.9. The RANS and Euler sim-

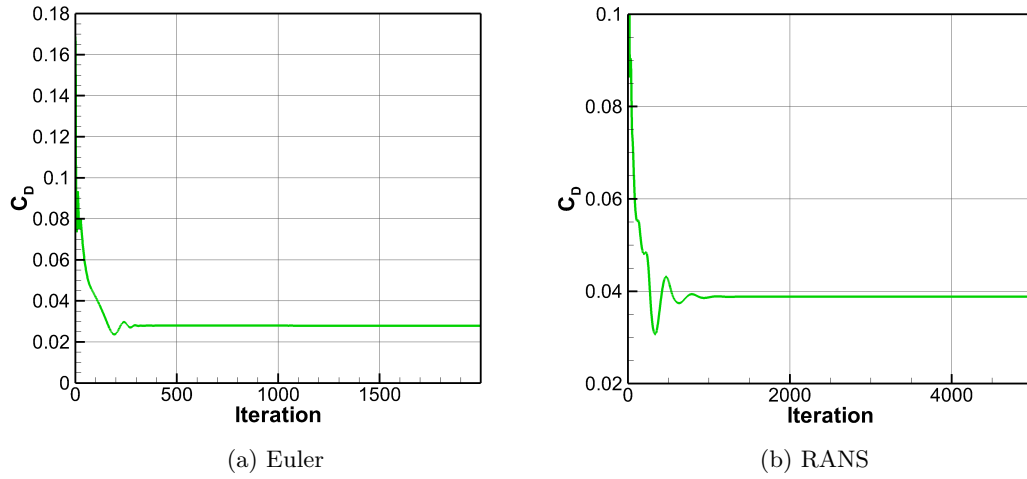


Figure 3.6: Drag convergence of sample simulations of the triangular tubercle wing for a Mach number of 0.83 and angle of attack of zero degrees.

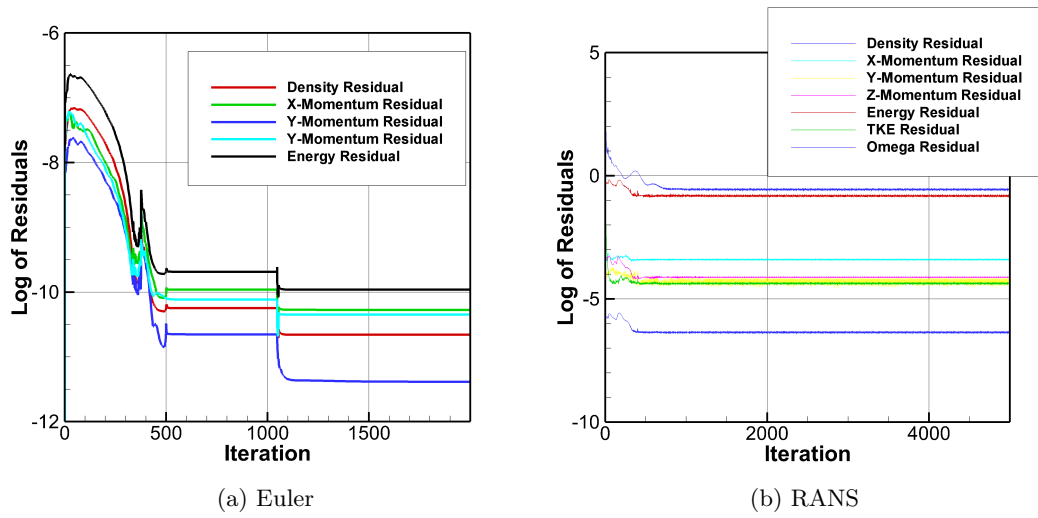


Figure 3.7: Residuals of sample simulations of the triangular tubercle wing for a Mach number of 0.83 and angle of attack of zero degrees.

ulation results indicate close agreement with the experimental data however with the Euler solution, the absence of SWBLI is evident from the larger pressure gradient across the shockwave which is clear with the pressure curve of Figure 3.9. Also, the small differences between the simulation from RANS and experimental curves can be explained with the change in Reynolds number. It was observed that the curves at $Re = 6.6 \times 10^6$ do not match as well as the ones at $Re = 3.0 \times 10^6$. At $Re = 6.6 \times 10^6$ the shockwave position is noticeably different but the curves in terms of shape and adverse pressure gradient appear almost identical.

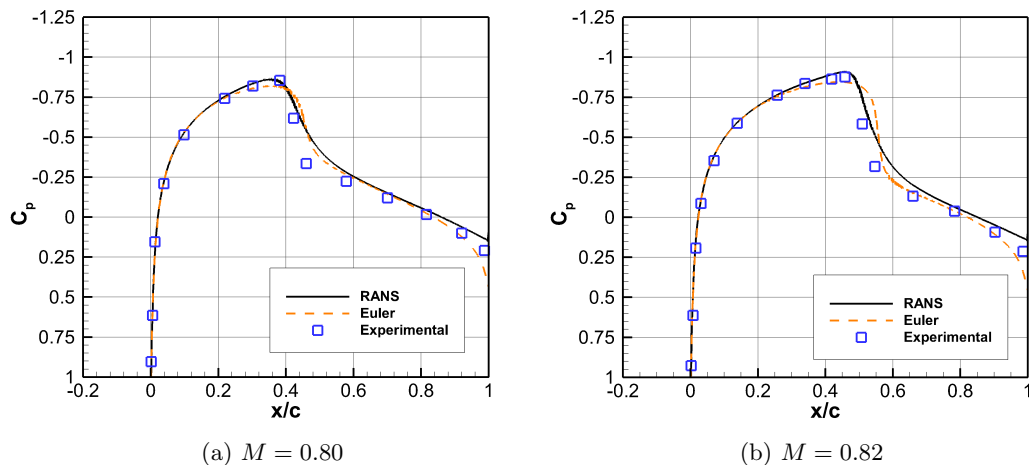


Figure 3.8: Simulated and experimental C_p curves ($Re = 3.0 \times 10^6$) [50] for the straight leading edge wing at two Mach numbers and angle of attack of zero degrees.

The NASA study from Noonan and Bingham [51] also documented the lift and drag of an NACA 0012 airfoil for a range of angles of attack, for a Mach number of 0.83 and a Reynolds number of 1.5×10^6 . The RANS simulation results were compared at an angle of two degrees and it was found that its lift coefficient of 0.2954 and drag coefficient of 0.0532 compares well with the NASA experimental lift of 0.3 and drag of 0.055. At zero lift, the drag does not correlate well, being 70 drag counts larger than expected (from 0.03 to 0.0374 which may be an indication of an over-prediction of the strength of the shockwave). This drag increase may be the result of having a lower Reynolds number, however, this drag was found to be in the range of values reported in a compilation of multiple NACA 0012 experiments as documented

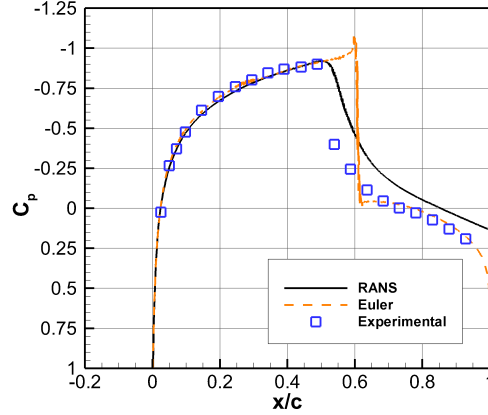


Figure 3.9: Simulated and experimental C_p curves ($Re = 6.6 \times 10^6$) [51] for the straight leading edge wing at Mach 0.83 and angle of attack of zero degrees.

in McCroskey [43]. The drag coefficient found in RANS was 0.0374 and the maximum drag at a Mach number of 0.83 in the NASA summary is around 0.04. The zero lift drag coefficient found using Euler is 0.0258 which is much lower than the one found using RANS and in McCroskey [43]. This indicates that with the Euler solution the strength of the shockwave is under-predicted. The considerable variation in the aerodynamic performance of the NACA 0012 in transonic flow is not surprising because of the unsteady nature of shockwaves. Despite this variation, it was decided that there was enough confidence in the results and representation of the flow characteristics from the simulation to move forward with the research.

3.6 Baseline Simulation Results

Once the simulation indicated close agreement to published experiments, the results were then examined and compared. This section presents and discusses the RANS simulation results of the three baseline wings: straight, triangular and sinusoidal leading edge. These simulations were done to establish a starting point in terms of drag and flow characteristics. Although the geometries and meshes were inspired from previous studies, they were recreated in the present simulations to eliminate the possibility of transferable errors. The meshes were also studied in more detail and refined with an exhaustive convergence study. The drag count results of the three wings are presented in Table 3.2. The two tubercled wing were found to have a higher drag than

the straight leading edge wing. For the triangular tubercle and the sinusoidal tubercle wing, the drag increases by 15 (4%) and 23 (6%) drag counts respectively. The increase in drag comes from an increase of the pressure drag as the friction drag varies very little even though the wetted area is increased with a tubercled wing. Since the main component of drag is pressure drag (around 92%), a drag reduction observed in Euler, a simulation that considers only pressure drag, should have similar improvements in RANS simulations and in experiments.

Table 3.2: Mach 0.83 drag count RANS results of the triangular and sinusoidal tubercle wing compared with the straight leading edge.

	Total Drag	Pressure Drag	Friction Drag
Straight leading edge	374	344	30
Triangular tubercle	389	360	29
Sinusoidal tubercle	397	368	28

The drag increase finding does not correlate with previous studies related to tubercles in transonic flow [6–10]. Thus, experimental work became a requirement to establish the validity of this trend and if the trend found in simulation can be explained in better terms than the possibility of RANS simulations having difficulty resolving the shockwave and complex SWBLI in transonic flow with additional flow features such as crossflow. Modifying the CFD setup such as changing the numerical scheme, the turbulence model and the characteristics of the mesh, varied the drag values but the trends always stayed the same. In every scenario, the triangular tubercle wing was found to have a higher drag than the straight leading edge wing. Note that the use of an alternative CFD solver was not attempted.

Even if the two initial tubercled wings were found to have a higher drag than the straight leading edge wing, a change from a sinusoidal to triangular tubercle shape did improve the drag by 8 drag counts meaning that an optimization on the tubercle shape was still worthy of further investigation. It is possible that the simulation of tubercles may not be accurate in relation to the straight leading edge but the optimization was still undertaken with the assumption that a performance gain obtained with a change in the shape of the tubercle may still have an overall improvement. The optimization process may still offer design insights but a comparison with the straight leading edge will have to be verified experimentally.

The pressure coefficient contours and curves of the straight leading edge wing and both original tubercle wings are shown in Figures 3.10, 3.11, and 3.12, respectively. The tubercled wings have a pressure gradient from the peak to the valley which could be the source of crossflow over the wing. The shape of the pressure curve of the triangular tubercle in the valley is similar to a Whitcomb type supercritical airfoil in terms of behavior with a very flat progression of the pressure until the shockwave [52]. The pressure contour shows that for both tubercled wings there is a larger negative pressure coefficient region right before the shockwave. The pressure coefficient curves of Figure 3.13, which present a close-up near the shockwave, show that both tubercled wings have a lower pressure right before the shockwave although the pressure gradient through the shock approximately remains the same. This is an indication of a higher Mach number immediately before the shockwave which leads to an increase in shockwave strength. This increase would by extension explain the drag increase.

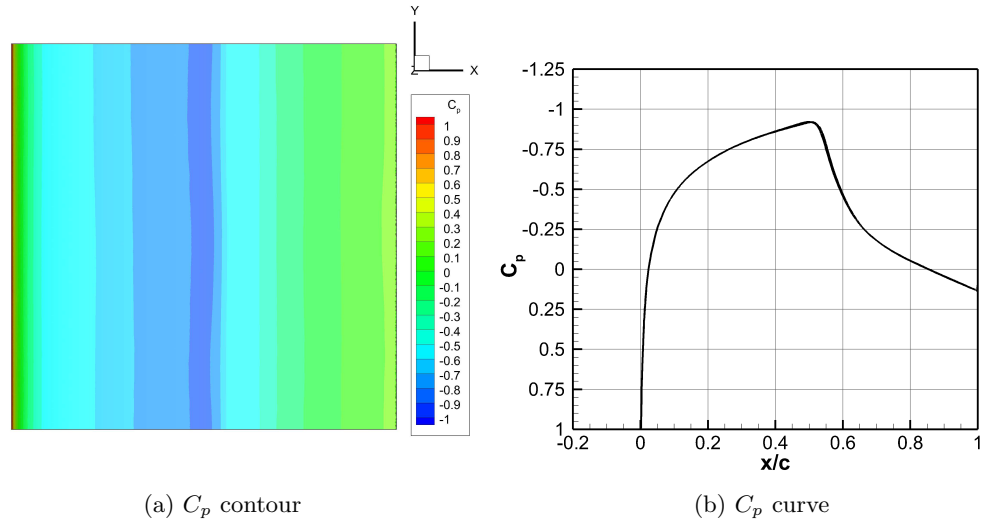


Figure 3.10: Straight leading edge wing simulated pressure at Mach 0.83.

It was initially theorized that a large valley region may be undesirable since the local larger thickness to chord ratio may have a negative impact on the overall transonic performance of the wing. For a straight leading edge wing, it is known that the thickness to chord ratio has an important impact on transonic performance, in fact, the drag divergence Mach number decreases with

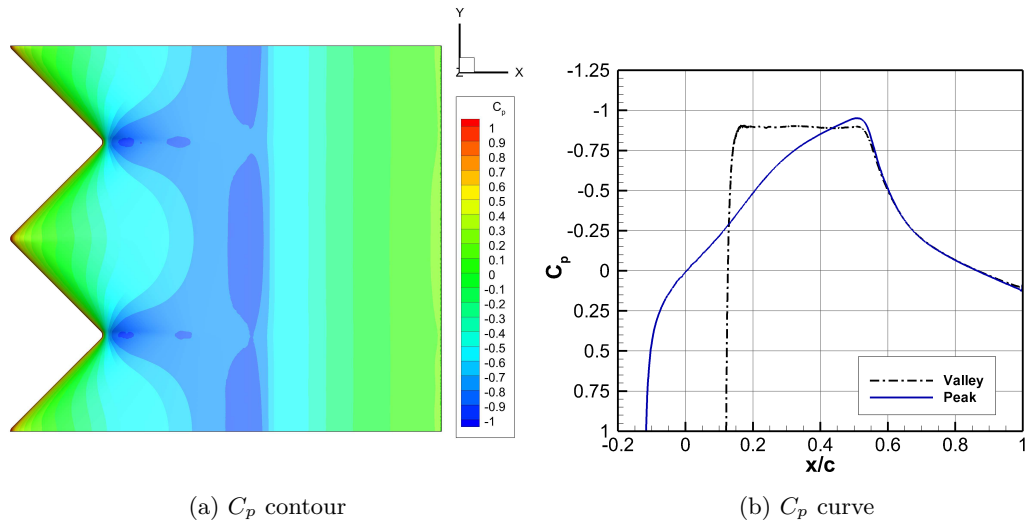


Figure 3.11: Triangular tubercle wing simulated pressure at Mach 0.83.

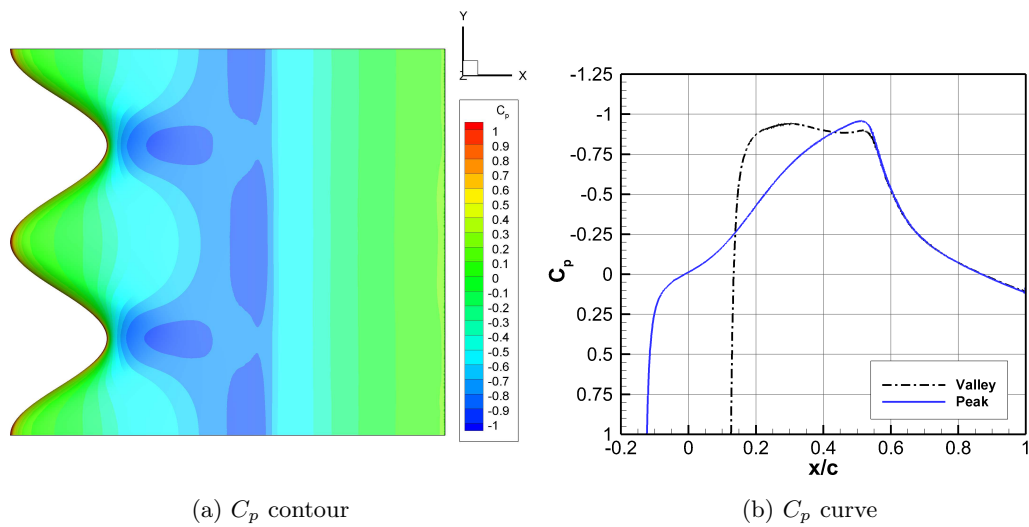


Figure 3.12: Sinusoidal tubercle wing simulated pressure at Mach 0.83.

an increasing thickness to chord ratio. This is due to the fact that thicker airfoils create higher supervelocities on the surface [4]. The flow over a thin wing is only slightly perturbed from the freestream creating a milder expansion

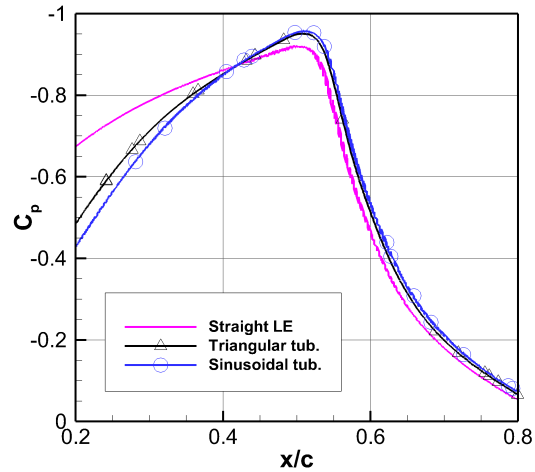


Figure 3.13: C_p curves of the two baseline tubercled wing compared to the straight leading edge in the shock region downstream of the peak.

over the wing [53]. Although this is true for a straight leading edge wing, this feature may not be locally applicable to a tubercled wing because of the 3D effects affecting the local performance. This is substantiated by the fact that there are higher local flow velocities after the peak and before the shockwave which does not correlate with a 2D change in thickness to chord ratio. The disadvantage of a large valley region is supported with the turbulent kinetic energy (TKE) and the turbulent viscosity which were visualized through CFD and are presented in the Annex, Section A.1. Those two simulation specific flow characteristics show the magnitude of perturbations in the flow and may indicate an increase in turbulence and losses. The magnitude of those two characteristics were found to be higher in the valley region.

The sinusoidal tubercle wing was disregarded as a starting point for the optimization because it has larger drag than the triangular tubercle wing and the remainder of the research is based on having a starting point with a triangular leading edge wing. Since the triangular tubercle wing has a larger drag when compared to the straight leading edge wing, it was decided to do a parametric analysis by changing the wavelength and amplitude of the triangular tubercle shape in order to preliminarily explore the design space and investigate the possibility of a better starting point for the optimization.

3.7 Initial Parametric Study

This parametric study was done to elucidate the impact of modifying the wavelength and amplitude of the triangular tubercle geometry. The wavelength and amplitude of the tubercles relate directly to the angle of the triangle. A change in this angle was thought to affect crossflow while the amplitude also affects the local thickness to chord ratio. The drag count results of the tested configurations are shown in Table 3.3. No clear trends were found in terms of wavelength and it was only found that as the amplitude was reduced the drag approaches the drag of the straight leading edge wing. Since none of the tested configurations was found to have a better drag than the straight leading edge wing, it was decided to keep the original triangular tubercle design as a starting point for the optimization and attempt an optimization with a smaller amplitude tubercle of the same wavelength to see if it can provide better results.

Table 3.3: Mach 0.83 drag count of the triangular tubercle wing with different wavelength and amplitude using a RANS solution.

$A \backslash \lambda$	$0.3c$	$0.5c$	$0.7c$
$0.10c$	379	379	376
$0.15c$	384	382	381
$0.20c$	384	384	383
$0.25c$	386	388	393

3.8 Constant NACA 0012 Tubercled Wing

In the search of a starting point with a lower drag than a straight leading edge, two more wings were investigated. The intention was to investigate wings that had the same airfoil and thickness to chord ratio spanwise when compared to a wing that stretches and compresses the airfoil chordwise to form the tubercles. As illustrated in Figure 3.14, two wings were designed to fit this constant airfoil criteria, the first one with a variable thickness but constant trailing edge and the second one with constant thickness and variable trailing edge. The leading edge tubercle shape is the same as the original triangular tubercle design.

3.8. Constant NACA 0012 Tubercled Wing

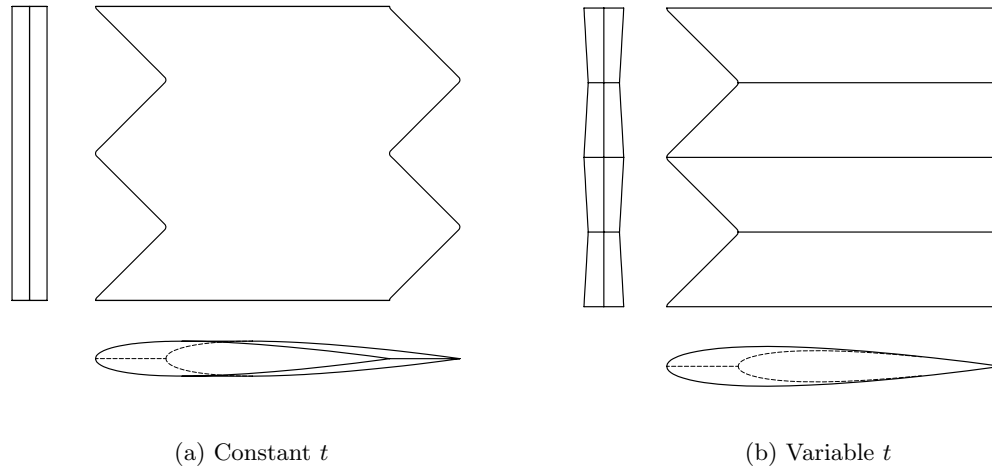


Figure 3.14: Constant NACA 0012 tubercled wings.

These two wings are only possible by allowing a wing that is different after maximum thickness when compared to the straight leading edge wing. The results can be compared to the straight leading edge because the average airfoil is the same even if the aft part of the wing is not the same. The drag count results are shown in Table 3.4 and it can be observed that both wings are able to improve drag from 4 (1%) to 22 (6%) drag counts when compared to the straight leading edge wing.

Table 3.4: Mach 0.83 drag count RANS results of two constant t/c triangular tubercle wings compared with the straight leading edge.

	Total Drag	Pressure Drag	Friction Drag
Straight leading edge	374	344	30
Variable t	370	341	29
Constant t	352	323	29

The pressure coefficient contours and curves of the two constant NACA 0012 wings are shown in Figure 3.15 and 3.16. When comparing to the straight leading edge wing, there is a reduction of the low pressure region immediately before the shockwave. Note that changing the airfoil shape at the valley of the baseline triangular tubercle wing to a NACA 0012 profile resulted in the pressure curve becoming very similar to the pressure curve of a peaky airfoil [52]. The reduction in the strength of the shockwave is probably due to a

combination of local sweep, the local position of maximum thickness (which means that crossflow and thickness-wise flow also have to be considered), the local airfoil shape and trailing edge shape.

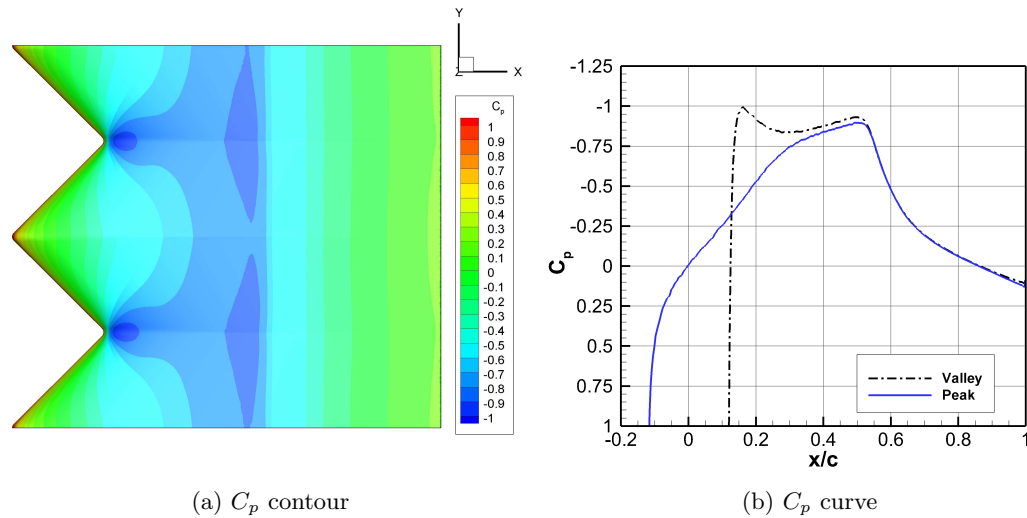


Figure 3.15: Variable thickness NACA 0012 tubercled wing simulated pressure at Mach 0.83.

It was first theorized that the origin of the pressure differential between the peak and the valley comes from a spanwise change in leading edge curvature but since the leading edge curvature is the same for the constant NACA 0012 tubercled wings and the pressure differential is still present, it is now thought that the differential is a result of sweep theory as applied to the tubercled wing leading edge. As the flow bifurcates at the peak, it brings the flow away from the peak and towards the valley. Another way to explain it is as the flow is divided at the peak, the chordwise flow velocity at the valley is higher than the velocity at the peak. This increased chordwise velocity would result in the sudden decrease of pressure at the valley. This flow decomposition can be seen with the streamlines near the leading edge of a triangular tubercle wing as shown in Figure 3.17.

Since optimizing the shape of the entire wing was not in the scope of this thesis, the wing shapes mentioned above were not considered as a starting point for the optimization. The two wings also have a spanwise discontinuity which led them to be considered as impractical structurally and impractical for manufacturing. Even if the two constant NACA 0012 profile tubercled wings

3.8. Constant NACA 0012 Tubercled Wing

were not investigated further they helped explain the origin of the pressure differential and show that the local airfoil shape can have an impact on the changes imposed by the presence of tubercles.

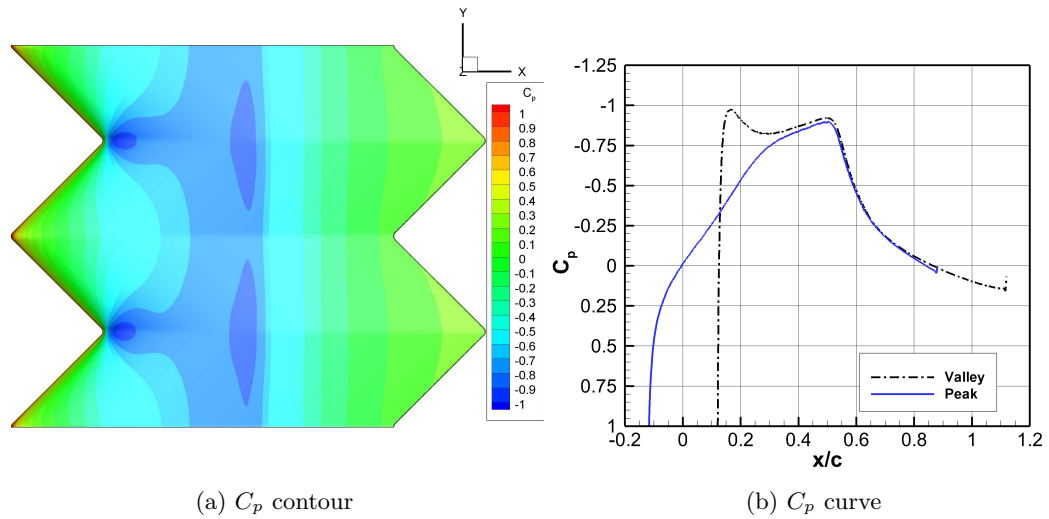


Figure 3.16: Constant thickness NACA 0012 tubercled wing simulated pressure at Mach 0.83.

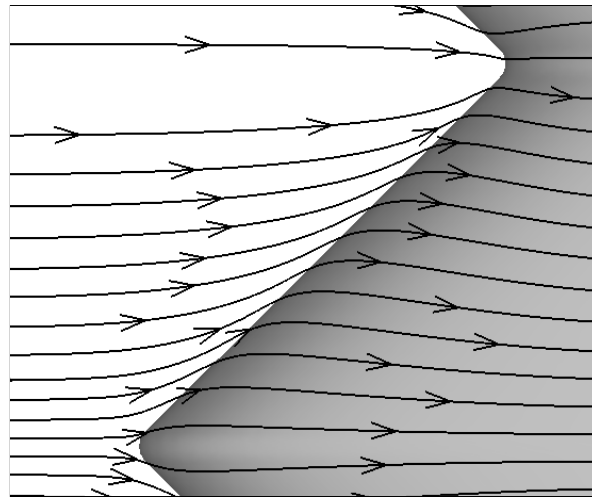


Figure 3.17: Streamlines near the leading edge of the triangular tubercle wing at Mach 0.83.

4 Optimization

In this chapter the details of the approach used to optimize tubercled wings are presented along with results from those efforts. An Euler-based aerodynamic shape optimization was followed by a post-optimal parametric study based on the new shape found by the optimizer which was done using RANS for increased analysis fidelity. The RANS simulation results of the final design were afterwards analyzed in further detail in order to elucidate flow features.

4.1 Optimization Problem

The optimization objective of this study was to minimize the drag coefficient of the triangular tubercle wing for a given Mach number (chosen to be 0.83) and at an angle of zero degrees. This angle was chosen to simplify the optimization and since only wings at zero degrees can be tested in the current experimental test section. The general formulation of the optimization problem is shown below.

$$\begin{aligned} \text{minimize : } & f(x_i, y_i) = C_D & (4.1) \\ \text{with respect to : } & x_i \quad i = 1, \dots n \\ & y_i \quad i = 1, \dots n \\ \text{subject to : } & x_{lb_i} \leq x_i \leq x_{ub_i} \\ & y_{lb_i} \leq y_i \leq y_{ub_i} \\ & g(x_i, y_i) \leq 0 \end{aligned}$$

The general formulation describes that the objective function of drag coefficient is minimized with respect to design variables (DV) in the x and y direction. Those design variables can be subject to a lower and upper bound, and one or multiple constraints. This optimization problem as applied on the wing was solved through aerodynamic shape optimization, which is a computational transformation of the shape in question guided with an optimization

algorithm in order to improve one or more aerodynamic characteristics. This type of optimization is able to directly modify the geometry of the body and is applied here to improve the tubercle shape.

4.2 Optimization Framework

The aerodynamic shape optimization process available as part of SU2 is utilized in this thesis as illustrated with the flow chart in Figure 4.1. The process starts with the definition of the starting point with a baseline geometry and mesh. This is also where the DVs are defined. A first CFD analysis is then completed to evaluate the objective function, f (which is drag in the case of this study). Afterwards, if gradient optimization is applied within the course of this process, a sensitivity analysis using adjoints is done for every objective and constraint, g . The gradient information is then verified for convergence with a user defined tolerance. If the criteria is met, a final design is provided, otherwise the gradient information is given to the gradient based optimizer in order to solve the optimization problem. The optimizer outputs new values for the DVs which are then applied as geometry and mesh deformation. The optimization cycle is then repeated iteratively until convergence is achieved. The following sections present more details about the tools used during every step of the optimization cycle.

4.2.1 Free Form Deformation Box

The DVs are defined when the mesh is built with the use of a Free Form Deformation (FFD) box. The FFD box encapsulates the geometry in a bounding box and a mapping is created between the FFD control points and the mesh surface nodes. Those control points, with a specific degree of freedom (x , y or z), become the DVs during the optimization as they control the shape of the surface grid. The box is then deformed by modifying the position of the control point and the contained surface inherits a smooth deformation [44]. For the deformation the mesh is treated as an elastic solid with a non-uniform stiffness, and the linear elasticity equations are then solved to obtain the displacement of the nodes with the movement of the control points as inputs [44]. The mathematical expression of how the Cartesian coordinates of the points of the surface of the object are transformed into parametric coordinates within the box can be found in Palacios *et al.* [44], and more details on the general FFD strategy can be found in Samareh [54]. An illustration of the box over the wing with triangular tubercles is shown in Figure 4.2.

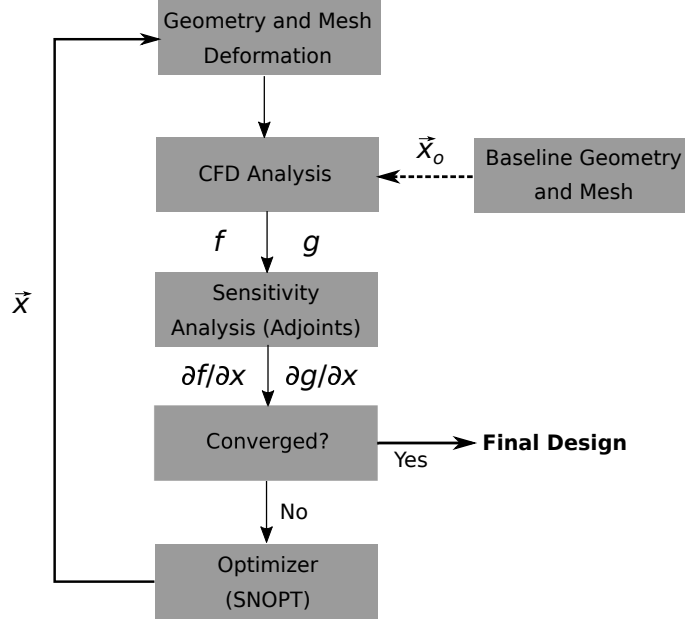


Figure 4.1: SU2 aerodynamic shape optimization process [44].

For the optimization of this study the FFD box is comprised of three layers of 20 chordwise by 30 spanwise control points to have a layer for the upper and lower surface of the wing and a layer at the center of the wing. The FFD box was sized in order to have no contact between the box and the boundaries of the simulation and the control points were positioned to have points along the tubercles in order to have an accurate mapping between the mesh and control points. In order to deform and optimize only the leading edge region, the optimizer was given the freedom to only move the control points closest to the tubercles. This is also done in order to minimize the exploitation of a reduction in thickness to chord ratio for a reduction in wave drag (wave drag is very sensitive to changes in thickness to chord ratio which is the clearest search direction for the optimizer) [4]. To minimize the number of DVs, only the control points of the middle FFD box layer and near the middle tubercle were used for the optimization, as indicated with Figure 4.3. Using the middle layer also ensured that the symmetry of the airfoil was kept intact without having additional constraints (which would add to the computational time). This made for a total of 17 control points. For the optimization of the tubercle shape, changes in the position of the FFD control points are allowed in the chordwise (x) and spanwise (y) direction, making for a total of 34 DVs.

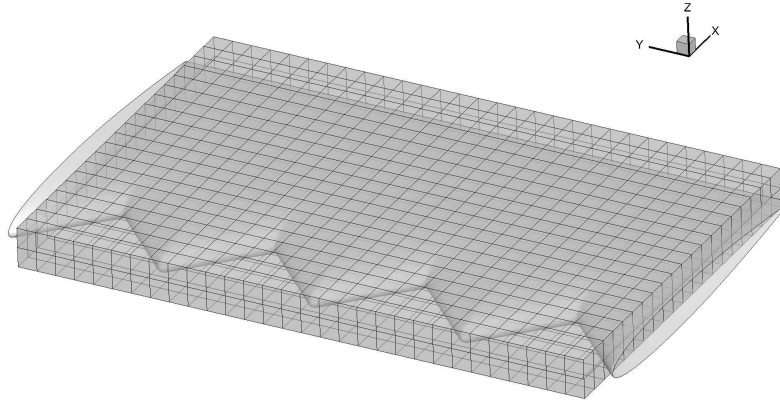


Figure 4.2: FFD box defined for the triangular tubercled wing.

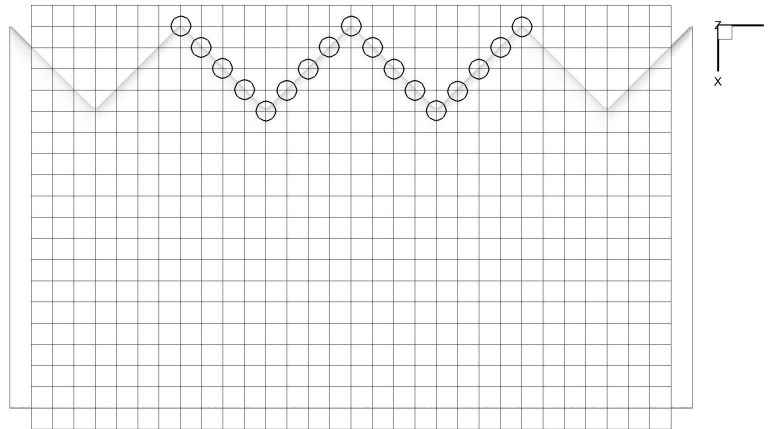


Figure 4.3: Top view of the FFD box defined for the triangular tubercled wing. The circled points indicate the control points that were kept for the optimization.

4.2.2 CFD Analysis

An Euler analysis was chosen for the simulation that evaluates the objective function during the optimization process. Euler was chosen because time was considered a priority to gain design insights and this type of simulation can capture pressure drag variations. Every optimization attempt involves multiple iterations which entails a simulation for the objective function and a sensi-

tivity analysis for every objective and constraint, all of which are much faster using Euler than when using RANS (for example a simulation in RANS took around 7.9hrs and Euler 0.6hrs on a computer cluster with 40 cores running at 2.67 GHz). The errors from the approximations in Euler were considered as acceptable because the Euler simulation is only used during the optimization process and finding an improvement was considered a higher priority at this stage than accuracy of the simulation. Also, as discussed in Section 3.6, the Euler simulation only considers pressure drag and a drag reduction in Euler should have similar improvements in RANS simulations. Verification of the potential improvements was conducted using RANS simulation after the optimization was conducted in Euler.

4.2.3 Sensitivity Analysis

In order to compute the gradients required by the gradient optimizer, two adjoint methods are available in SU2, the continuous and discontinuous adjoint. The adjoints are a method to obtain gradients with the use of residuals [55]. In the context of this study, those gradients represent the sensitivity of the impact of small changes for the DVs on the objective function and constraints which is the sensitivity of shape deformation to the flow solution. A general mathematical description of adjoints can be found in Mader *et al.* [55] and the implementation of the adjoint method in the SU2 software can be found in Palacios *et al.* [44]. For this optimization the continuous adjoint method was chosen because it is about 25% faster than the discontinuous adjoint method with its current implementation in SU2 while it also converges to the same values [55].

4.2.4 Optimization Algorithm

With the sensitivity information readily available, gradient optimizers can be used as the optimization algorithm. Gradient optimizers use sensitivity information to find a search direction and take a step of a predefined length towards the minimum that they identify which is how new values are given to the DVs.

The optimization algorithms SNOPT (Sparse Nonlinear Optimizer) and NLPQLP (NonLinear Programming with Non-Monotone and Distributed Line Search), implemented in the pyOpt package integrated in SU2, were used in this study [56]. SNOPT is an optimizer that uses a sequential quadratic programming (SQP) method and it is able to solve large-scale nonlinear optimization problems with thousands of constraints and DVs [57]. The NLPQLP

optimizer, which is another type of algorithm that uses an SQP method, was only used when it was attempted to apply geometrical constraints to the wing. SNOPT is a more aggressive optimizer that explored beyond the constraints whereas NLPQLP was able to respect them.

4.3 Optimization Results

The intent of the optimization shown in this section was to deform the tubercle shape as much as possible in order to see if any hints could be found for an improvement of the shape. To allow that, the wing deformation was not geometrically constrained, the upper and lower bounds of the DVs were not bounded and the convergence criteria was set to 1×10^{-13} . This means that the cycle and deformations will continue until the optimization converges, is manually stopped, or the mesh reaches its deformation limit where the cells become so skewed that the CFD run starts to diverge. The entire optimization took 72 hrs to complete.

4.3.1 Optimization Convergence

The progression of the drag coefficient during the optimization is shown in Figure 4.4 and the corresponding change in tubercle shapes obtained from sample optimization iterations is illustrated in Figure 4.5. The convergence rate of the optimization is shown in Figure 4.6 and it indicates that the optimization has a quadratic type convergence, which is expected of an SQP type method, and that the optimizer is approaching a local minimum because of the rate advancing towards zero. The optimization was stopped once a tolerance of 2×10^{-5} was reached on the drag coefficient. At that point the optimization also reached the deformation limit of the mesh. When looking at the optimized tubercle shape, there is evidence that increasing the thickness to chord ratio is the shape characteristic with the most sensitivity with regards to drag. Even if the average chord of the wing is increased, the local chord is increased more at the peak than at the valley which is an indication of a shape sensitivity with regards to the tubercle amplitude. Another shape characteristic was observed as soon as iteration 10 which consists of a curvature on the tubercle sides. It was decided to investigate in more detail the shape at iteration 10 because of the large increase in chord evident in further iterations. This shape already provides a considerable reduction of 32 drag counts (in Euler) for a small shape modification. This large decrease was suspected to be mainly caused by the increase in chord but the change in tubercle shape was found to

be worthy of further investigation. Note that an increase in chord is not desirable for this study because this type of transformation changes the average airfoil shape, planform area and maximum thickness location, and the effect of adding tubercles to a wing cannot be compared to the performance of the straight leading edge wing. It was established that in order to compare wings with tubercles to a wing with a straight leading edge, the same average chord, maximum thickness, and average maximum thickness location is required.

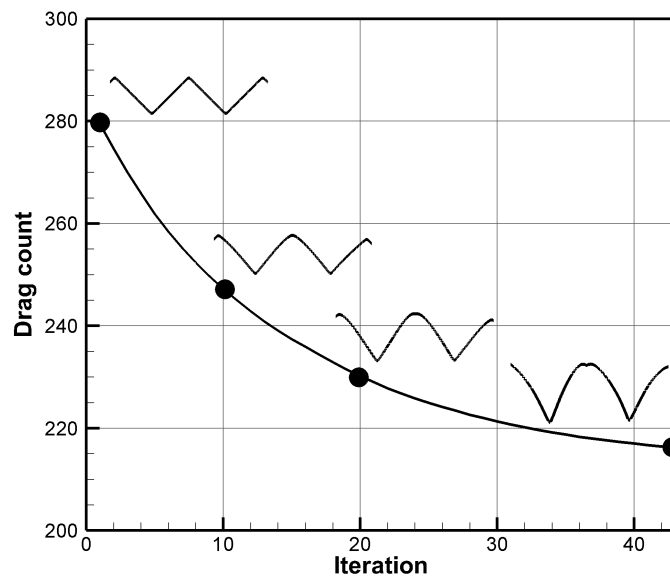


Figure 4.4: Objective function history.

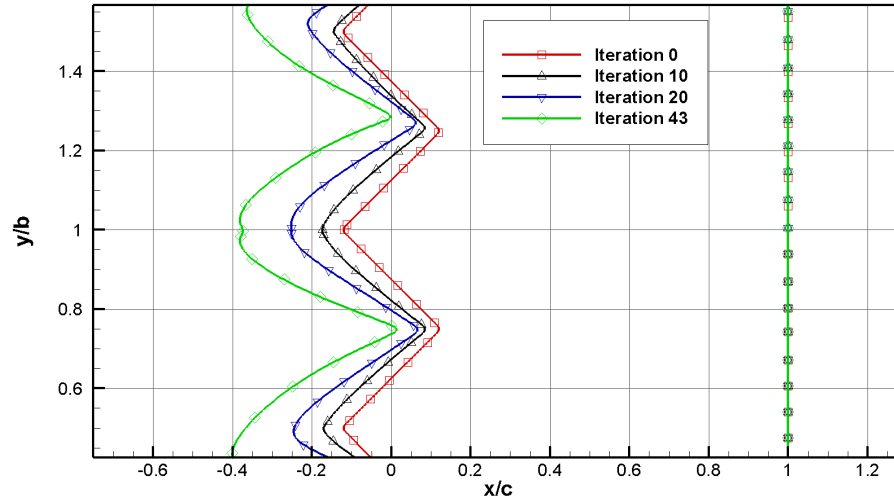


Figure 4.5: Original triangular tubercles and optimized tubercle shapes of three sample iterations.

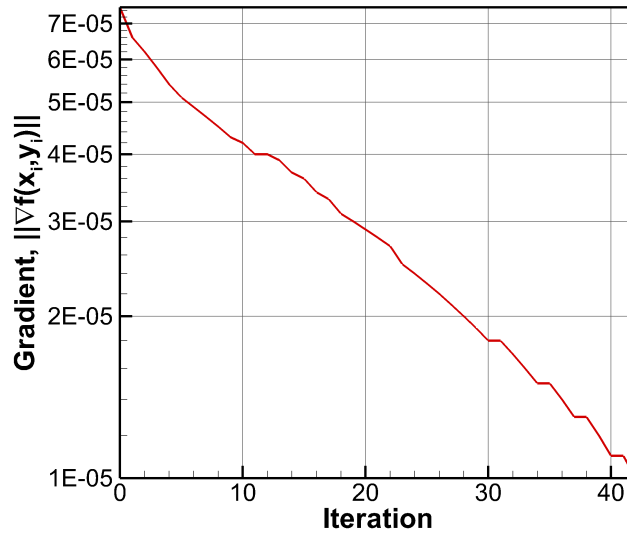


Figure 4.6: Convergence rate history.

4.3.2 Shape Parametrization

For further examination, the shape of the tubercle was recreated from the output of the optimization at iteration 10. As presented in Figure 4.7, the curvature of the tubercle was found to closely resemble the shape of the power series function given by:

$$y = \frac{\lambda}{2} \left(\frac{x}{A} \right)^n \quad (4.2)$$

A power value of $n = 0.75$ was found to closely match the shape found by the optimizer. This power series was applied to the triangular tubercle wing and adjusted in terms of average chord to match the chord of the straight leading edge wing. The recreated wing is shown in Figure 4.8. Further analysis of the optimal shape represented by the power series was done using RANS to account for viscosity effects and SWBLI. With RANS, the power $n = 0.75$ shape was found to have an improvement of 7 drag counts over the triangular tubercle design. This improvement initiated the idea of increasing the curvature of the tubercle by decreasing the power value of the parametrized shape described in Equation 4.2.

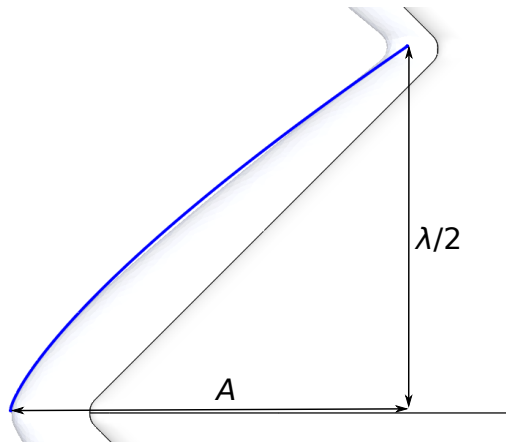


Figure 4.7: Illustration of a power function fitting ($n = 0.75$) on the optimized tubercle shape of iteration 10.

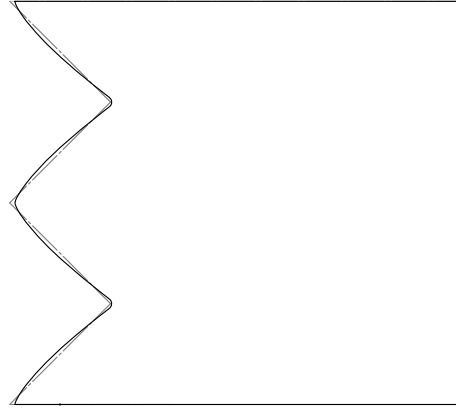


Figure 4.8: Power $n = 0.75$ tubercles (the dotted lines show the original shape).

4.4 Tubercle Shape Parametric Study

Upon the original optimization results a post-optimal parametric study was performed using tubercle shapes represented by the power series of Equation 4.2. The power was reduced from $n = 0.75$ to $n = 0.10$, producing shapes as shown in Figure 4.9. Two other tubercle shapes, elliptical and Von Karman, were investigated based on the idea of an outwards curvature. Note that all investigated tubercle shapes are inspired from low drag missile nose shapes [58, 59]. The two alternative shapes were calculated based on Equation 4.3 and 4.4, and are shown in Figure 4.10 (note that the curves were translated to start from the same point as shown in the graph). All tubercle shapes were corrected in terms of average chord to match the original straight leading edge wing. The results of this parametric study are found in Table 4.1 and 4.2 and it can be seen that the lowest drag value is with a power of $n = 0.20$. This shape pushes the outwards curvature which further promotes the flow characteristics that will be discussed in Section 4.6. Reducing the power any further starts bringing the shape back towards a straight leading edge, thus increasing the drag of the wing. Another contribution to the increase of drag for the power $n = 0.10$ shape is a small amplitude reduction because of the small fillet that is added to the valley of every wing.

$$y = \frac{\lambda}{2} \sqrt{1 - \frac{x^2}{A^2}} \quad (4.3)$$

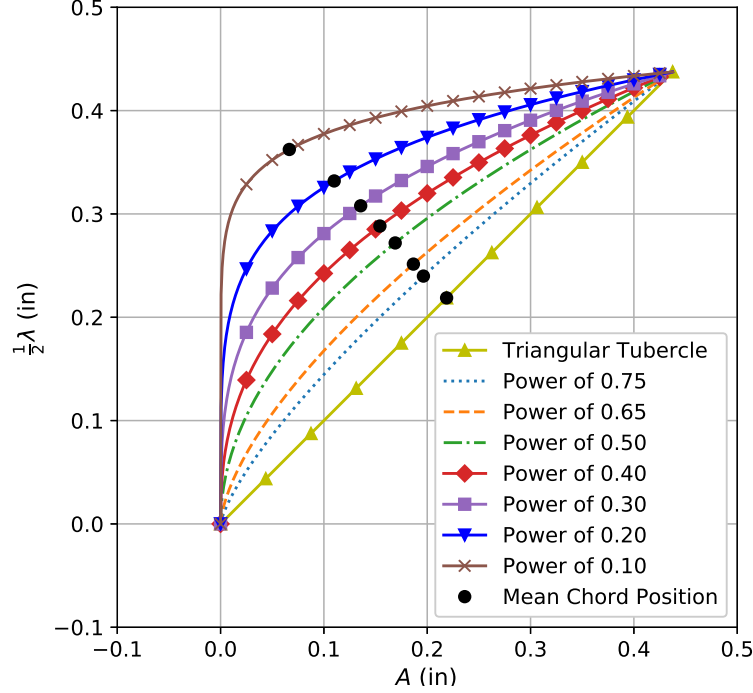


Figure 4.9: Graph of sample power functions applied on tubercles.

$$y = \frac{0.5\lambda}{\sqrt{\pi}} \sqrt{\theta - \frac{\sin(2\theta)}{2}} + C \sin^3(\theta) \quad (4.4)$$

$$\theta = \arccos\left(1 - \frac{2x}{A}\right)$$

$$C = 0, \quad \text{if Von Karman nose shape}$$

With the best shape, power $n = 0.20$, the design space was explored further by changing the amplitude and wavelength but that led to no further improvements in aerodynamic performance. A reduction of amplitude led to an increase in drag, and the shape was less sensitive to a variation in wavelength with only a slight drag increase. The results of this analysis can be seen in Table 4.3. It was decided to limit the amplitude to 25% of the chord length in order to keep the same airfoil shape after maximum thickness. Ultimately, it was found that the power $n = 0.20$ shape at a wavelength of $0.5c$ and an amplitude of $0.25c$ provides the best performance in terms of drag.

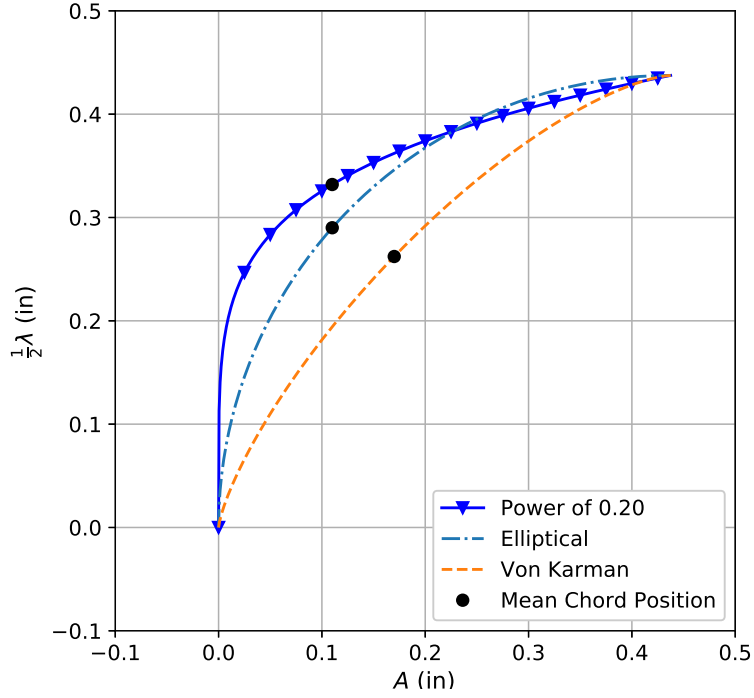


Figure 4.10: Graph of alternative shape functions applied on tubercles.

Table 4.1: Drag count results for the parametric study of the power series.

Power	Drag counts
1.00	389
0.75	382
0.65	378
0.50	369
0.40	363
0.30	354
0.20	351
0.10	356

Table 4.2: Drag count results for the parametric study of alternative shape functions.

Shape	Drag counts
Elliptical	365
Von Karman	369

Table 4.3: Mach 0.83 drag count results of the power $n = 0.20$ with different wavelength and amplitude.

$\lambda \backslash A$	$0.3c$	$0.5c$	$0.7c$
$0.2c$	363	361	363
$0.25c$	356	351	353

4.5 Optimization Result Sensitivity

Other optimizations were performed to investigate the sensitivity of the optimization result with regards to changes in flow conditions, starting geometry, bounds and constraints. The trend of an outward curvature, and especially an increase in average chord, was present in most cases. For example by increasing the Mach number to 0.9, the only difference was that the objective function was more sensitive to geometrical changes which simply resulted in a more deformed shape quicker. The opposite was observed by lowering the Mach number to 0.75 meaning that the optimization resulted in a less deformed shape. A change in starting geometry was done by optimizing a triangular tubercle wing with a lower amplitude ($0.10c$). The optimization process provided a shape with more marginal improvements when compared to the optimization done on a tubercled wing with a larger amplitude, although the trend of outward curvature was still present. The same trend was observed when bounds of $0.07c$ was applied during the optimization but a convergence was reached quickly as the shape reached the limit giving a shape very similar to the one of iteration 10.

When the wing was volume constrained, the increase of average chord was completely eliminated. The geometrical constraint that would have been the most relevant for this study would be to constrain the planform area which is

not currently an option for aerodynamic shape optimization in SU2. To work around this issue it was possible to use a volume constraint because the planform area of a wing only being deformed in x and y will be near constant if the volume is constrained. In order to respect this constraint, the tubercle shape ended up being deformed in a different way. The peak was pinched while the outwards curvature near the valley was increased. The optimal shape of that effort was recreated for simulation in RANS giving the shape illustrated in Figure 4.11. This new shape improved the drag by 7 drag counts when compared to the original triangular leading edge wing but this shape was left aside because its improvement was lower than geometries used in the parametric study.

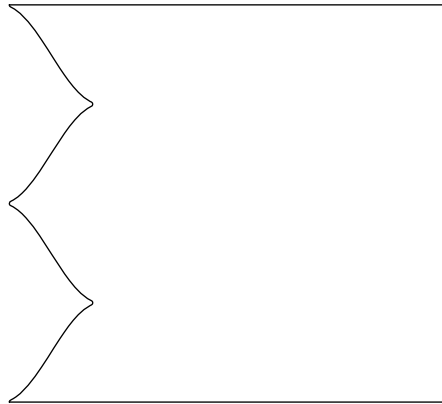


Figure 4.11: Planform surface sketch of the recreated wing from an optimization with constant volume constraint.

A thickness-wise optimization allowing changes in local airfoil shape was also undertaken. This resulted in an improvement by reducing the leading edge radius especially at the valley. This was an indication that changing the airfoil shape spanwise can improve drag behavior but without means to compare this change to the straight leading edge wing, the idea was not explored any further. The optimum power $n = 0.2$ was used as an initial solution of an additional optimization. However, no further improvement was obtained verifying the local optimum nature of the shape.

4.6 Flow Analysis of the Optimal Transonic Tubercle Shape

With the power $n = 0.20$ tubercle as the optimal shape, the simulation results and flow features were investigated in order to elucidate reasons for the improvement. From the RANS flow analysis it was found that, at a freestream Mach number of 0.83, the optimized wing reduced the drag by 23 drag counts when compared to the straight leading edge. A summary of the drag count results for the straight, triangular and power $n = 0.20$ leading edge wings are presented in Table 4.4. Similar to the triangular leading edge wing (see Section 3.6 for details on the simulation), the change in drag of the power $n = 0.20$ leading edge wing comes from a variation of the pressure drag, while the friction drag seems to remain unchanged. This was the first indication of a reduction in shockwave strength.

Table 4.4: Mach 0.83 drag count results of the power $n = 0.20$ compared with the baseline and triangular tubercle.

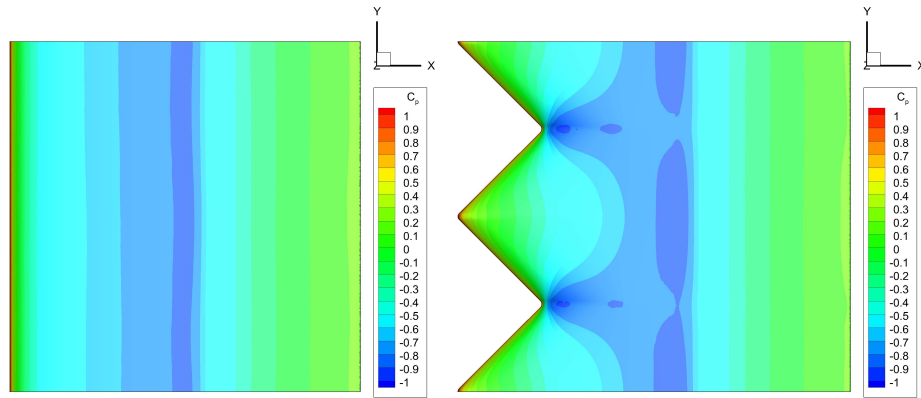
	Total Drag	Pressure Drag	Friction Drag
Baseline	374	344	30
Triangular tubercle	389 (+4%)	360	29
Power $n = 0.20$	351 (-6%)	323	29

¹ The value in the bracket is the percent relative difference from the straight leading edge wing.

The surface pressure contours of the power $n = 0.20$, triangular and straight leading edge wings are shown in Figure 4.12. The C_p contours show a spanwise variation of pressure between the peak and the valley in both tubercled wings, which correlates with previous studies. As mentioned in the study of Perez and Asghar [8], this pressure variation indicates that there is an expansion of the flow in a direction other than chordwise which alters the formation and strength of the shockwave. The power $n = 0.20$ shape also constricts the chordwise region of lower pressure to be more local to the valley and the spanwise region of lower pressure before the shockwave is reduced for this wing when compared to the two other shapes.

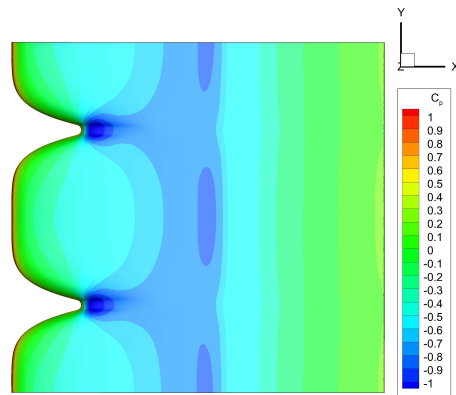
The chordwise behavior can be observed with the C_p curves shown in Figure 4.13. A feature of the power $n = 0.20$ shape is that the valley has a very similar behavior to a peaky airfoil, characterized by a suction peak near the leading edge followed by a near constant progression of the pressure until the shockwave [52]. This peaky behavior is similar to what was shown for the tubercled

4.6. Flow Analysis of the Optimal Transonic Tubercle Shape



(a) Straight leading edge

(b) Triangular



(c) Power $n = 0.20$

Figure 4.12: C_p contours of three wings at Mach 0.83.

4.6. Flow Analysis of the Optimal Transonic Tubercle Shape

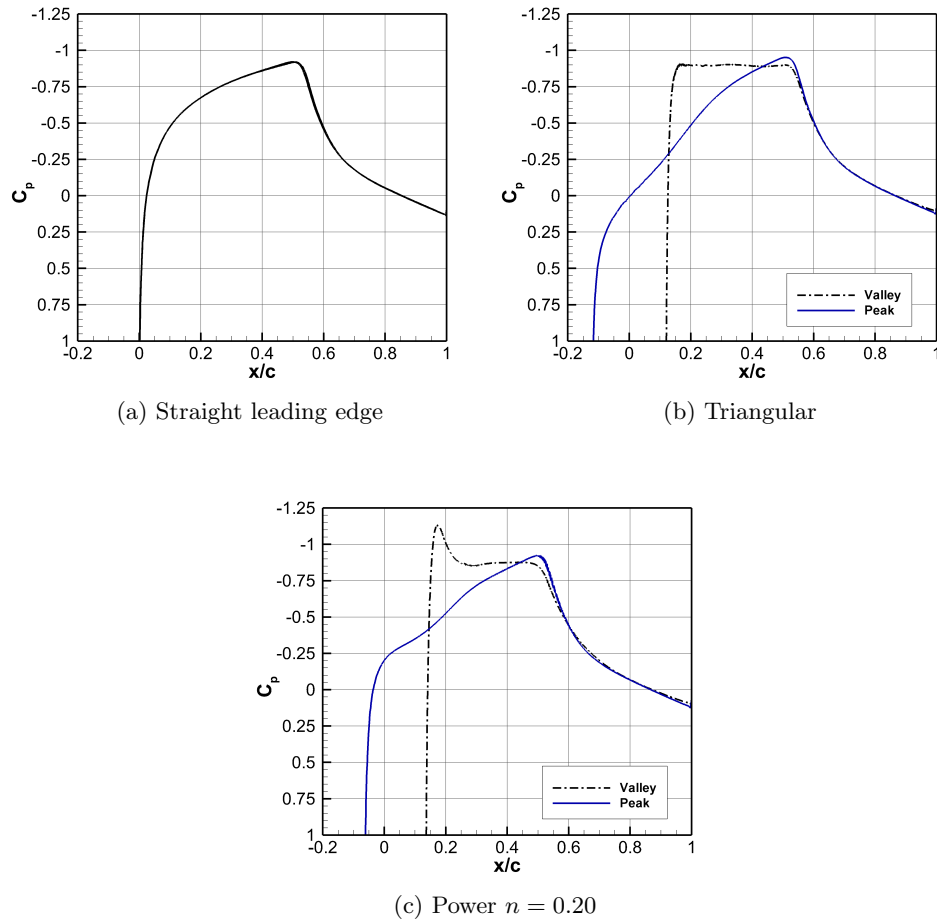


Figure 4.13: C_p curves of three wings at Mach 0.83.

wings with constant NACA 0012 airfoil as shown in Section 3.8 although the reason for its appearance in the case of the power $n = 0.20$ wing is driven more by the tubercle shape than the local airfoil shape. In the power $n = 0.20$ shape, this suction peak can indicate that there is more crossflow near the valley. The increase of the magnitude of crossflow can be visualized with the increase in friction coefficient in the spanwise direction when comparing the power $n = 0.20$ to the triangular wing as seen in Figure 4.14. This suction peak is also related to the flow velocity over the wing as the flow reaches a high velocity of Mach 1.44 in that region (compared to the maximum Mach number of 1.27 at the valley of the triangular leading edge wing). This velocity cannot be sustained because the airfoil at the valley is not shaped to be able to maintain or even re-accelerate the flow afterwards. This would then lead to a reduction of shockwave strength if the Mach number prior to the discontinuity has a lower magnitude when compared to the two other wings. This is evident when the behavior is compared to the tubercled wings with constant NACA 0012 airfoil described in Section 3.8 where the flow is re-accelerated after the suction peak, which is related to the local position of maximal thickness. The C_p curve at the valley of the power $n = 0.20$ shape, as shown in Figure 4.15, shows a reduction in shockwave strength. In fact, there is an increase in C_p right before the shockwave (which can be an indication of a lower Mach number prior to the start of the shockwave) and a more gradual pressure gradient across the shock. Note that no significant migration of the shockwave was observed, hence the gain in performance comes from the presence of a weaker shockwave. The flow velocity over the wing can also be visualized with the Mach number contours as shown in Figure 4.16 and a lower Mach number region before the shockwave can be observed for the power $n = 0.20$ leading edge wing (this is more evident in the valley region).

The suction peak at the valley of the power $n = 0.20$ shape comes from an acceleration of the flow in the valley because of a spanwise contraction coming from the new shape. This phenomenon can be visualized with the streamlines in the valley of the power $n = 0.20$ leading edge wing as shown in Figure 4.17. Also, the increase in flow velocity in the valley can be visualized with the Mach contour ahead of the leading edge in Figure 4.18.

4.6. Flow Analysis of the Optimal Tubercle Shape

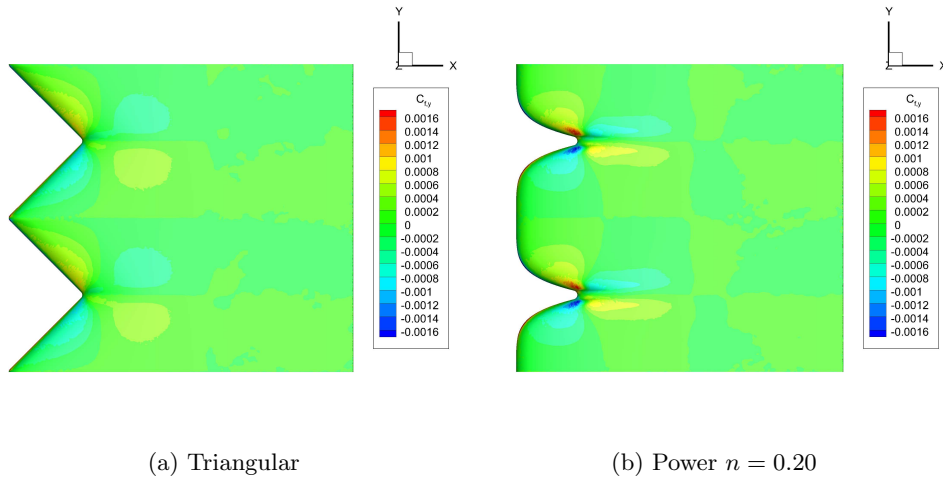


Figure 4.14: Spanwise friction coefficient of two tubercled wings at Mach 0.83.

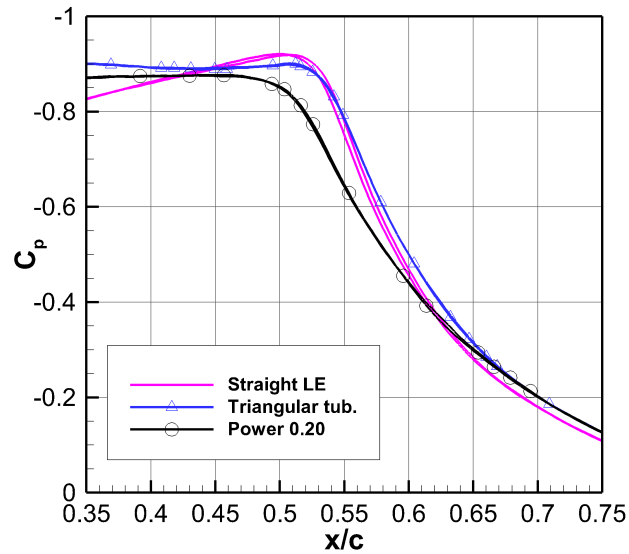
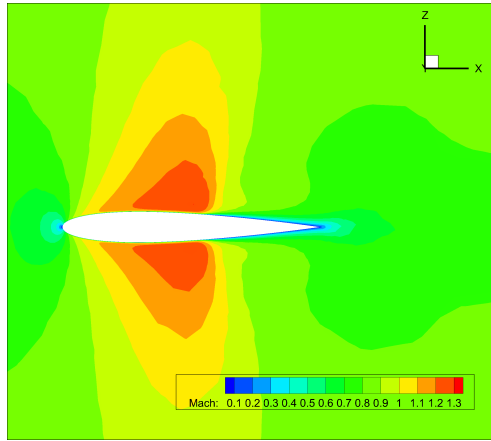
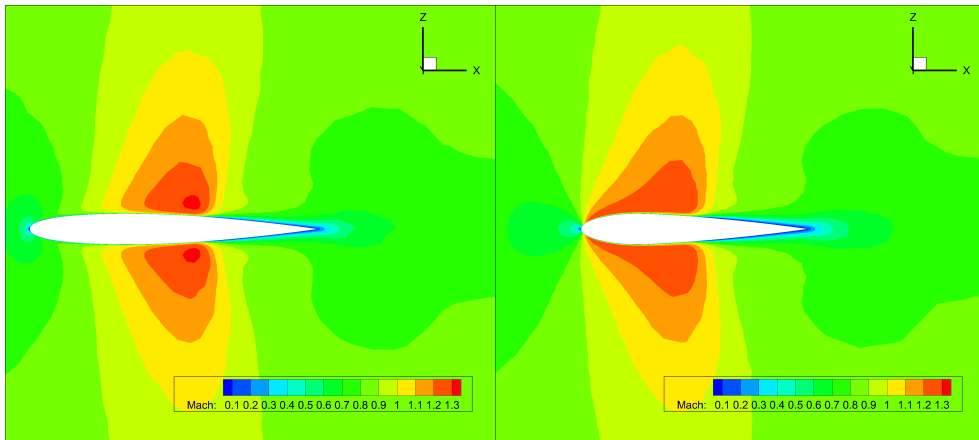


Figure 4.15: C_p curves of the two tubercled wing compared to the baseline in the shock region of the valley.

4.6. Flow Analysis of the Optimal Transonic Tubercle Shape

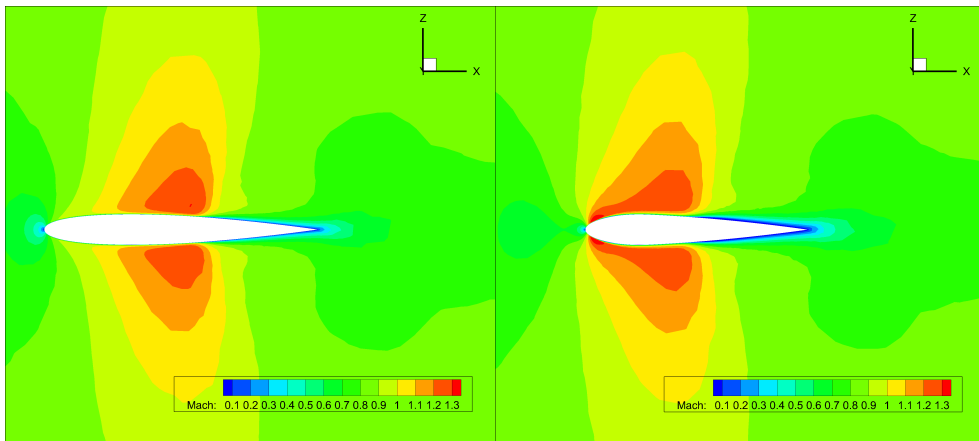


(a) Straight leading edge wing



(b) Triangular tubercle peak

(c) Triangular tubercle valley



(d) Power $n = 0.20$ tubercle peak

(e) Power $n = 0.20$ tubercle valley

Figure 4.16: Mach number contours of three wings at Mach 0.83.

4.6. Flow Analysis of the Optimal Transonic Tubercle Shape

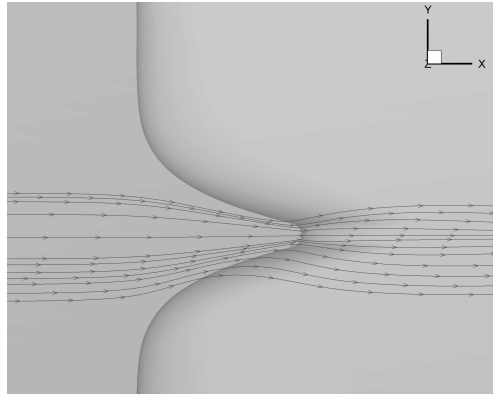


Figure 4.17: Streamlines in the valley of the power $n = 0.20$ leading edge wing at Mach 0.83.

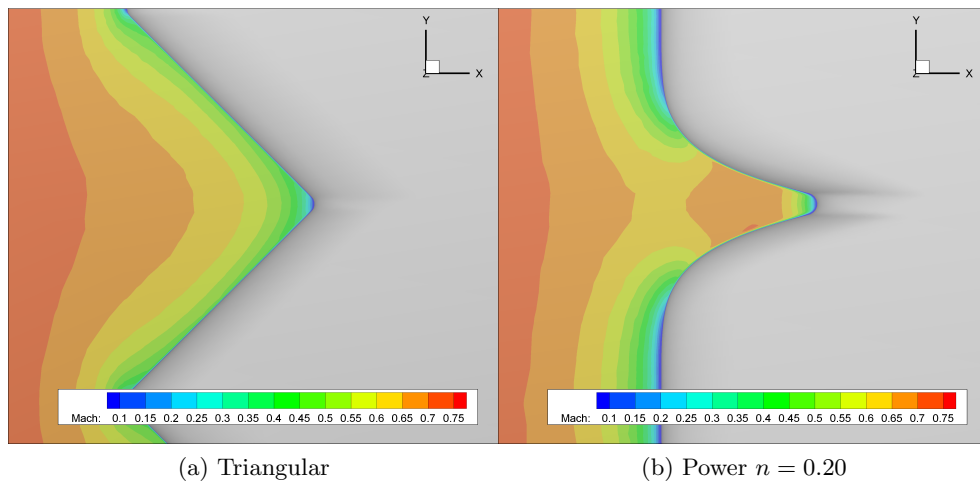


Figure 4.18: Mach number contour in front of the leading edge of two tubercled wing at a freestream Mach number of 0.83.

Examining the boundary layer is also useful for an additional explanation regarding the drag improvement of the power $n = 0.20$ leading edge wing. Even if less full boundary layer profiles such as those having experienced roughness or previous adverse pressure gradient can separate more easily, those same flow cases also have a larger upstream influence and more shock smearing at its base which can reduce the adverse pressure gradient and can reduce the sensitivity of the flow to downstream pressure rise [60]. In the case of the power $n = 0.20$ leading edge wing the suction peak prior to the shock thickens the boundary layer which contributes to a weaker SWBLI. This is seen with the Mach contours shown in Figures 4.19 and 4.20. Those contours show a thickening of the boundary layer at the valley of tubercled wings as opposed to the thinner boundary layer at the peak and with the straight leading edge wing. In summary, the power $n = 0.20$ shape has a better aerodynamic performance in terms of drag because it has a peaky behavior at the valley which promotes more crossflow and a lower Mach number prior to the shockwave. The shape also limits the penalty due to the lower chord of the valley.

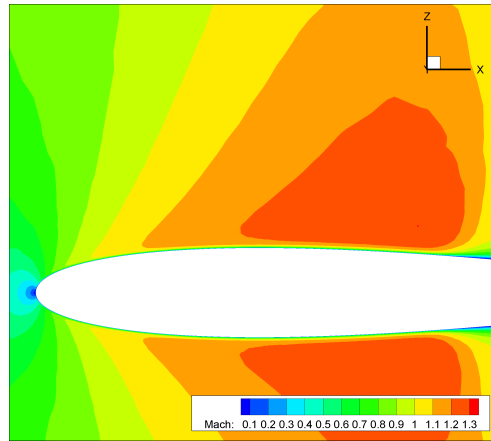


Figure 4.19: Mach number contour close up of the straight leading edge wing at Mach 0.83.

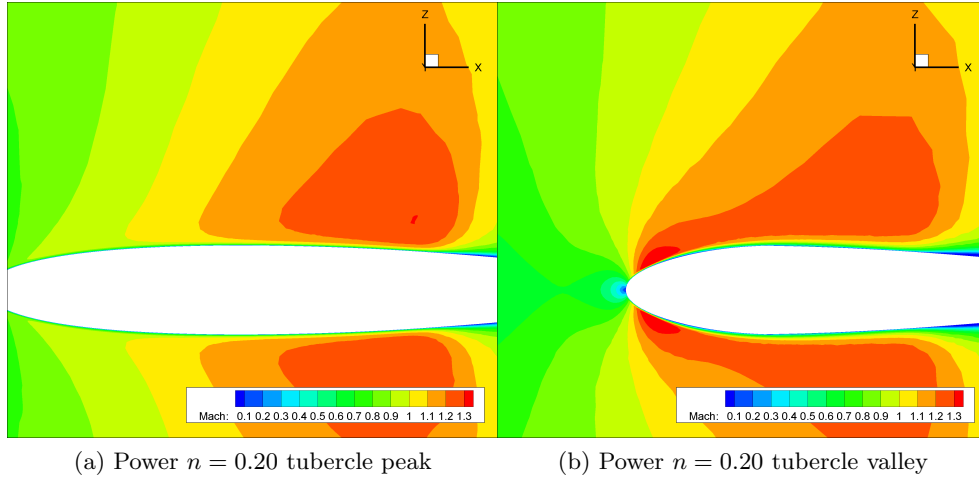


Figure 4.20: Mach number contour close up of the power $n = 0.20$ tubercle wing at Mach 0.83.

4.6.1 Angle of Attack Performance

A preliminary investigation to have a sense of the possible performance variations at an angle of attack of wings with tubercles was performed. A summary of the aerodynamic performance, computed using RANS, of the power $n = 0.20$, triangular and straight leading edge wing is shown in Table 4.5. It was found that the presence of tubercles creates a loss of lift at both examined angles, for example, the lift is 15% lower for the power $n = 0.20$ leading edge wing when compared to the straight leading edge wing at an angle of attack of two (2) degrees. The aerodynamic efficiency of both tubercle wings is also lower because of this large loss of lift but the power $n = 0.20$ leading edge wing is able to maintain a higher efficiency than the triangular tubercle wing as it has a large drag improvement. The drawback was not experimentally validated as part of this thesis but should be something to keep in mind for any possible application of tubercles.

4.6. Flow Analysis of the Optimal Transonic Tubercle Shape

Table 4.5: Mach 0.83 aerodynamic performance results at two angles of attack for the power $n = 0.20$ compared with the baseline and triangular tubercle.

	C_L	C_D	C_L/C_D
AOA = 1°			
Straight leading edge	0.1738	0.0422	4.12
Triangular tubercle	0.1526 (-12%)	0.0428 (+1%)	3.57 (-13%)
Power $n = 0.20$	0.1506 (-13%)	0.0394 (-7%)	3.82 (-7%)
AOA = 2°			
Straight leading edge	0.2954	0.0532	5.56
Triangular tubercle	0.2675 (-9%)	0.0526 (-1%)	5.08 (-9%)
Power $n = 0.20$	0.2511 (-15%)	0.0490 (-8%)	5.12 (-8%)

¹ The value in the bracket is the percent relative difference from the straight leading edge wing.

5 Experiments

This chapter presents the approach and results of an experimental campaign done to support the computational results and verify the performance and flow features of the optimal tubercle shape found during the optimization campaign. Three types of experiments were done in a transonic wind tunnel. Force measurements with a load cell were done to evaluate performance differences and pressure measurements and surface flow visualization were recorded to investigate flow characteristics.

5.1 Methodology

5.1.1 Experimental Setup

Experiments to investigate the effect of the optimized tubercle shape at an angle of attack of zero degrees were done in an indraft transient polysonic wind tunnel at RMC. As a point of comparison, experiments were also done on the triangular and straight leading edge wings. As shown in Figure 5.1, the wind tunnel consists of an inlet, test section, throttling valve, diaphragm-rupture mechanism and a vacuum tank. The tunnel functions by depressurizing the tank close to vacuum conditions and this vacuum is held with a thin gasket seal at the rupture disc. Once the gasket is ruptured there is a sudden pressure differential between the ambient air and vacuum inside the tank. There is then a sudden air flow, with 0.5 s of steady state, that passes through the test section in order to bring equilibrium.

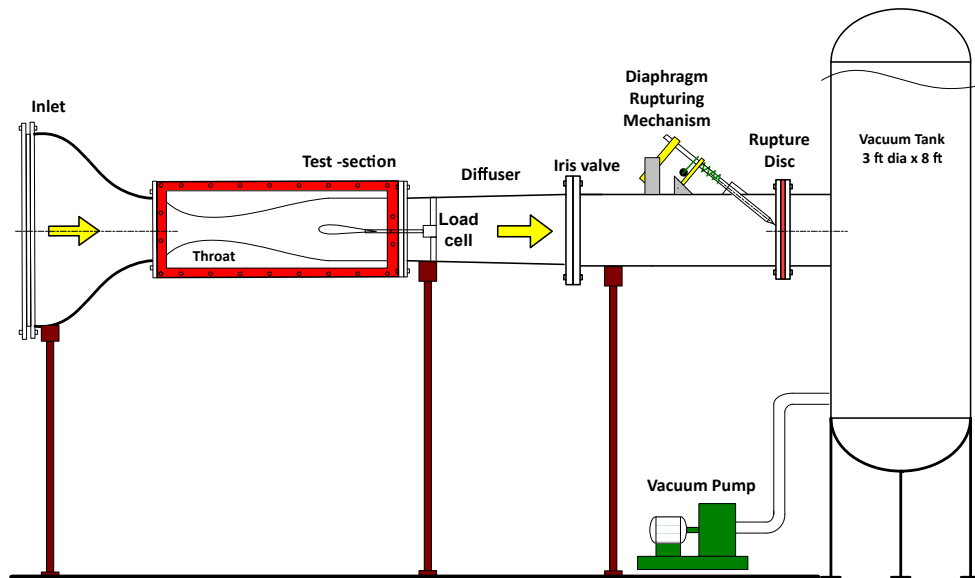


Figure 5.1: Indraft transient polysonic wind tunnel schematic [6].

A constant area duct test section (with a height of 3.2in and a width of 2in), as shown in Figure 5.2, is used downstream of a convergent nozzle which provides transonic flow using an aft iris valve with an adjustable diameter that defines the area ratio of the test section in order to control the flow velocity. The duct walls of the test section were adjusted to provide a constant area above and below the wings while also accounting for boundary layer growth on the surface of the wing [7]. It is important to have a constant duct area above and below the wing in order to ensure that the local area does not impact the local flow velocity and that the flow chokes at its intended location. With the current test section and iris valve setup the maximum freestream velocity is a Mach number of 0.84.



Figure 5.2: View of the test section.

For each experiment, the freestream velocity in the test section was measured using surface pressure taps installed on the test section wall directly in line with the mid span of the wing. The wings' surface and wall pressure were measured using an array of 16 pressure sensors housed in a *Scanivalve DSA3217* pressure scanner module. The full scale of pressure sensors is 15 psig and the accuracy is $\pm 0.05\%$ full scale. The pressure scanner has an integrated (16 bit) A/D converter, and the signals were sampled at 500 Hz per transducer. The Tygon tubes combined with the Scanivalve and A/D converter have a response time of less than 80ms [7]. The Mach number was calculated from the atmospheric and freestream static pressure with the following equation [61]:

$$\frac{p_{atm}}{p_{\infty}} = \left(1 + \frac{\gamma - 1}{2} M_{\infty}^2\right)^{\frac{\gamma}{\gamma - 1}} \quad (5.1)$$

$$M_{\infty} = \sqrt{5 \left(\left(\frac{p_{atm}}{p_{\infty}} \right)^{0.4/1.4} - 1 \right)} \quad (5.2)$$

5.1.2 Force Measurements

Force measurements with a load cell were done in the wind tunnel in order to experimentally measure the effect of tubercles and their shape on the drag of a NACA 0012 based wing. The load cell is a *ATI-IA Nano25* 6-axis strain gage based transducer and the data acquisition was done with a 16-bit DAQ recording data at a sampling frequency of 10 000 Hz. The *Nano25* has a 250 N range in the x and y direction and 1000 N in the z direction. For the moments, the range is 6 Nm in the x and y direction and 3 Nm in the z direction. With this calibration, the resolution is 1/24 N in x and y , and 1/8 N in z and for the moments, 1/660 Nm in x and y and 1/1320 Nm in z (the axis system of the load cell defines the x direction as the thickness-wise direction, y as the spanwise direction and z as the chordwise direction). This load cell was chosen in order to have a load cell with a diameter that would minimally affect the flow to limit the possibility of blockage and be capable of handling large loads while the newly designed load cell setup is tested, established and troubleshot.

To measure the forces, the load cell was positioned behind the wing and the wing was fixed via a sting as illustrated in Figure 5.3. Note that there is an uncertainty on the angle of attack of up to 0.1 degree (estimated from the measured lift) although very low angles have a negligible impact on the drag [51]. A fairing was added over the sting in order to eliminate the drag of the face of the load cell. This can be seen by comparing Figure 5.3 to Figure 5.4. Note that there is a small part of the sting that is still visible to the flow. This will add to the measured drag of the wing but will not affect a comparison between different wings.

The wing models have a span of 1.97 in (50.0 mm) and a chord of 1.75 in (44.5 mm). These models span the width of the test section with a clearance of 0.015 in (0.4 mm) on each side of the wing for ease of installation. The wings were made from plastic using a polyjet high definition rapid prototyping machine (*Object3DPro*) and the surface of the printed wings were sanded manually using fine grade sandpaper to have a roughness height on the wing of $Ra = 1$ to $2 \mu\text{m}$ [6].

To ensure repeatability, the procedure for the force measurements was to record drag 5 times at the same velocity for two wings to establish a difference between the straight leading edge and a tubercled wing. This was repeated a second time on a separate day to verify that the ambient air conditions and starting with a specific wing did not impact the difference. The

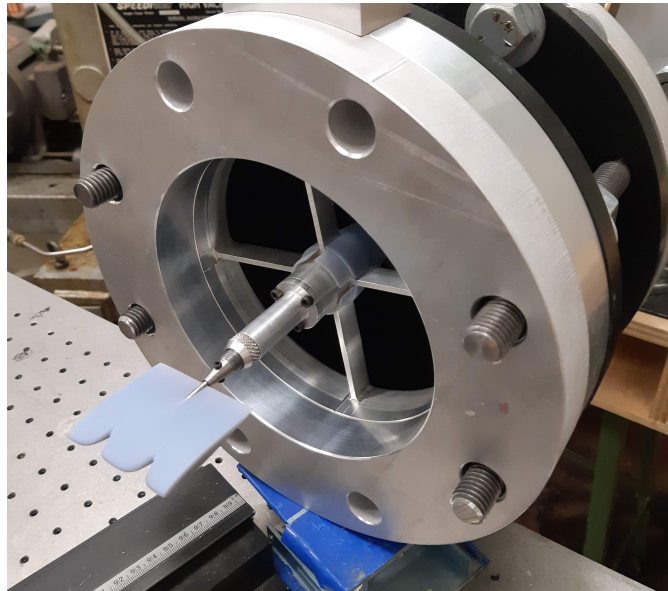


Figure 5.3: Wing fixture for the load cell.

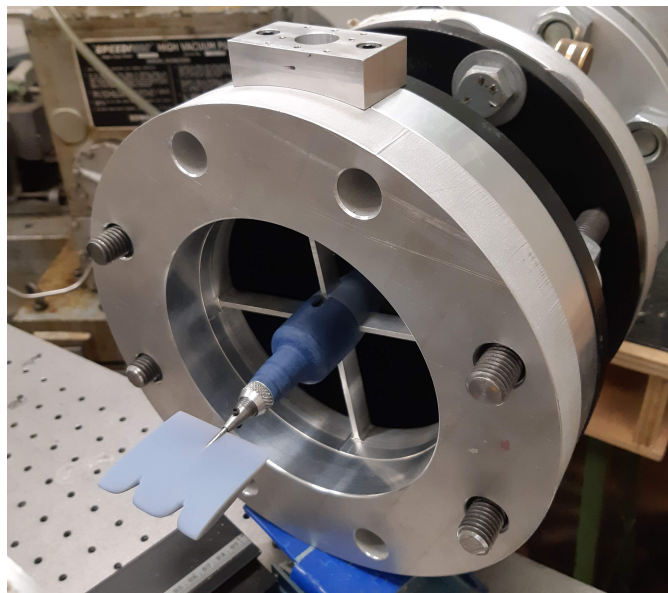


Figure 5.4: Wing fixture for the load cell with fairing.

test was done 5 times at the same conditions because it was found that the first measurement for a given wing was around 0.1 to 0.3N lower than the fairly consistent following measurements. The issue of the first measurement is suspected to be because of a response time of the load cell, and several measurements were required to have confidence and take into account the dynamic nature of the load. This response time is not indicated in the load cell specification although it is shown to exist in Bajo and Simaan [62] for small loads relative to the tested load cell range. Verification of this fact in the context of this experiment requires further testing. It was only when looking at the drag differences between wings that a consistent trend could be established because the drag force varied up to 8% from one day to another even at the same freestream velocity. This is most likely because of varying initial conditions such as ambient pressure and temperature that can affect the formation, interaction and strength of the shockwave in the transonic regime near drag divergence.

With this procedure, tests were performed around Mach 0.81 (while the wings are compared at the same velocities, obtaining an exact velocity of Mach 0.81 is difficult with the current experimental setup and a variation of ± 0.005 on the velocity was considered acceptable). It was decided to pay particular attention to this Mach number because it was estimated that the largest difference between the three wings is when the drag starts to diverge. This was established during preliminary measurements where the drag was very similar between the wings before Mach 0.79 and after Mach 0.83. Before Mach 0.79 tubercles may not create significant enough flow features to create a difference and after Mach 0.83 it is theorized that the drag divergence curves start to merge to a single curve with very similar drag (this is most likely due to limited leading edge effects when a strong shockwave is close to the trailing edge). The drag at higher velocities becomes hard to quantify and compare between wings because of its large sensitivity to small changes in Mach number. All these conclusions were reached when it was attempted to measure the drag force at multiple velocities in order to capture the drag rise and a graph showing a compilation of all the drag force measurements is included in the Annex, Section B.1 (The inconsistencies from the first measurement and between days are not differentiated in the graph). Note that the Mach number of every other experiment (pressure measurements and flow visualization) was selected to be between Mach 0.82 and 0.83 to capture more clearly flow characteristics. In order to calculate the drag differences the measured drag force was normalized using the following equation:

$$C_D = \frac{F_z}{0.5\rho U_\infty^2 S} \quad (5.3)$$

where,

$$\rho = \frac{p_{atm}}{RT} = \frac{p_{atm}}{287 \frac{\text{J}}{\text{kg K}} T} \quad (5.4)$$

$$U_\infty = M_\infty a \quad (5.5)$$

$$a = \sqrt{\frac{\gamma p_{atm}}{\rho}} = \sqrt{\frac{1.4 p_{atm}}{\rho}} \quad (5.6)$$

5.1.3 Surface Pressure Measurements

Surface static pressure measurements were carried out for the optimal and straight leading edge wing at multiple chordwise location as shown in Figure 5.5 and 5.6. The pressure measurements were also done at different spanwise positions corresponding to the peak, valley and mean line (coincident with straight leading edge locations). The pressure taps were integrated to the wing models via a rapid prototyping machine, by generating internal channels extending from the wing surface to the edge of the model. Tygon tubes were connected to these channels through stainless steel tube inserts. The thickness of the wing allowed only for 6 pressure ports per side and the pressure was measured with the *Scanivalve DSA3217* as described in Section 5.1.1. The wings have a span of 2 in (50.8 mm) and 1.75 in (44.5 mm) of chord and the models span the entire width of the test section. To calculate the pressure coefficient the following equation was used:

$$C_p = \frac{p_s - p_\infty}{0.5\rho U_\infty^2} \quad (5.7)$$

and in terms of Mach number,

$$C_p = \frac{\frac{p_s}{p_\infty} - 1}{0.5\gamma M_\infty^2} \quad (5.8)$$

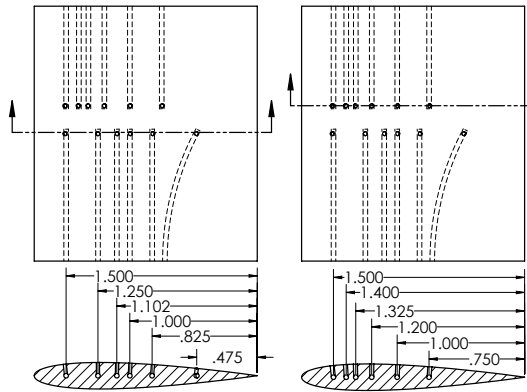


Figure 5.5: Straight leading edge wing pressure tap locations in inches [7].

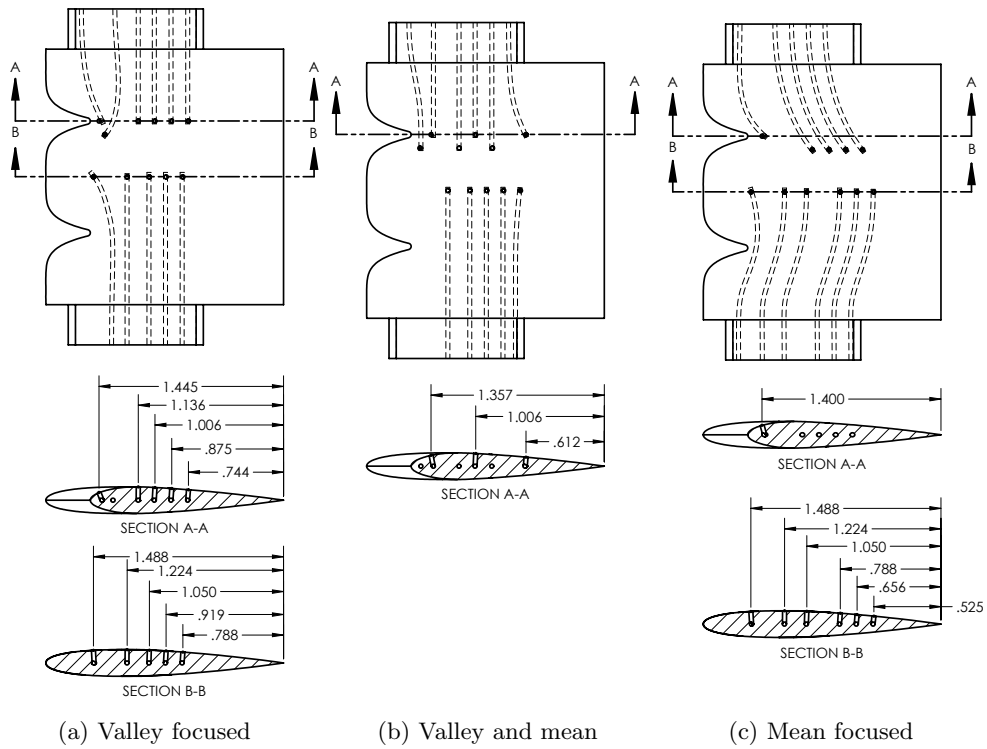


Figure 5.6: Power $n = 0.20$ wing pressure tap locations in inches (taps at the mean location are at the same chordwise positions as taps at the valley).

5.1.4 Surface Flow Visualization

Surface flow visualization was carried out on the same models that were used for pressure measurements (except without the pressure taps) to observe flow features such as shockwave position, and boundary layer and spanwise flow interactions. A mixture of isopropyl alcohol and AeroShell aviation oil was used and the ratio of the two compounds was determined by a trial and error procedure to obtain the best flow patterns at the selected flow speed. To observe the surface flow patterns, a 450 nm blacklight (UV-A) lamp was used to utilize the fluorescent characteristic of aviation oil. The alcohol in the mixture allowed for the formation of fine droplets on the surface and reduced the mixture viscosity for increased interaction with the flow. For testing, the models were sprayed with the mixture using a pneumatic spray gun. During testing the flow patterns were captured by video recorded under blacklight. The accumulation and location of the oil during the tests indicated the flow patterns and regions of separated, stagnated, or shock flow [7].

5.2 Experimental Results

The drag differences between the tubercled wings compared to the straight leading edge wing are shown in Table 5.1. The drag differences obtained from CFD at a Mach number of 0.81 were also added to the table. From the table it can be observed that the optimal wing is able to reduce drag around 13 drag counts (representing an improvement of 6%) and the triangular leading edge wing is shown to increase drag of around 6 drag counts. The trends correlate with the findings in CFD, although the differences vary slightly because CFD simulates an infinite wing while experimental data was affected by the presence of the walls. The total drag has an uncertainty of ± 6 drag count which leads to the conclusion that the optimal tubercle shape is able to reduce drag and that the loss of performance of the triangular tubercle wing needs to be confirmed with more precise load cell measurements.

The surface pressure measurements at Mach 0.825 are shown as a C_p curve in Figure 5.7 and as a C_p contour in Figure 5.8 and Figure 5.9. For the power $n = 0.20$ leading edge wing, the behavior in terms of C_p is very similar to what was observed in CFD (see Figure 4.13). The suction peak is evident with C_p values reducing quickly to around -1.2 right at the leading edge of the valley meaning that there is a very large pressure differential between the peak and the valley and that the wing profile at the valley has a peaky behavior (although a better resolution of pressure taps would be required to

Table 5.1: Drag count comparison of two tubercled wings to the straight leading edge wing using experiments and CFD.

Tubercle shape	Mach number	$\Delta C_D (\times 10^{-4})$
Triangular	0.806	+6
Triangular	0.813	+7
Triangular CFD	0.810	+11
Power 0.20	0.807	-14
Power 0.20	0.815	-13
Power 0.20 CFD	0.810	-15

better characterize the peaky behavior). The SWBLI starts around $0.4c$ with C_p values around -1 . At this chordwise location the C_p prior to the shock and the pressure gradient is slightly lower at the valley than the peak; both phenomenon are also present in CFD (see Figure 4.13). Since the pressure taps at the mean point are included in the experimental C_p contour, it can be seen that the suction peak is very local to the valley and that the SWBLI is different between the peak and the valley. A similar difference in SWBLI was observed in CFD (see Figure 4.12) although the difference is more prominent experimentally.

The general experimental behavior is similar to CFD but the C_p values and the shockwave location does not exactly match what was predicted in CFD. In CFD the suction peak reaches a minimum C_p value of -1.14 and the C_p value right before the shockwave reaches a minimum of -0.92 at the peak and -0.88 at the valley while in experiment the minimum C_p value is -1.2 and the C_p is -1 right before the shockwave. It is true that the C_p values are not too far off but the shockwave location is not at the same place at all with its occurrence starting at $0.4c$ vs $0.5c$ in CFD. These differences can be explained with the fact that experimentally the wing interacts with the test section in multiple ways. For example, in the test section there are walls and the simulation only considers an infinite wing. The area progression of the test section was designed to have even flow throughout the test section with a straight leading edge NACA 0012 wing which may not remain true with a tubercled wing. It was observed during schlieren imaging, an example of which is shown in Figure 5.10, that at the beginning of the area correction on the upper and lower wall there is evidence of oblique shockwaves and boundary layer separation that can change how the flow interacts with the wing especially since this boundary

layer separation will affect the area progression around the wing. Schlieren visualization was done on tubercled wings and the straight leading edge wings and the experimental setup schematic and sample images of the results are included in the Annex, Section B.2. Note that the schlieren experiment did not give any quantifiable differences between the shockwaves of the wings which is why the results are not included in this section.

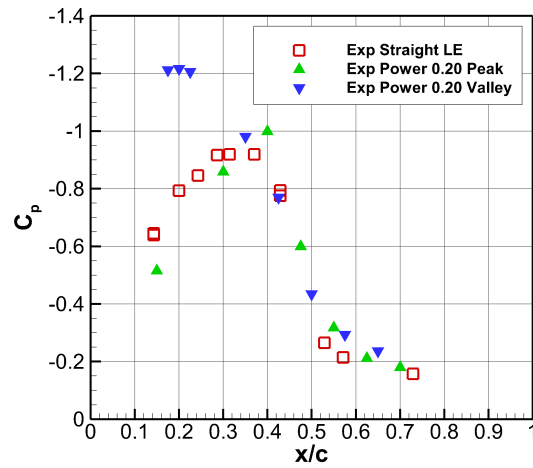


Figure 5.7: Experimental C_p curves of the power $n = 0.20$ and straight leading edge wing at Mach 0.825.

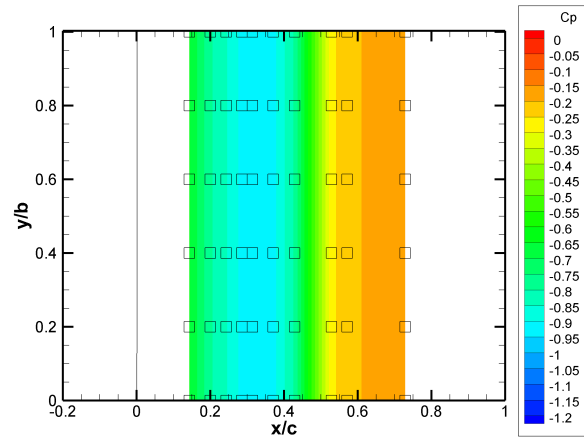


Figure 5.8: Experimental C_p contour of the straight leading edge wing at Mach 0.825.

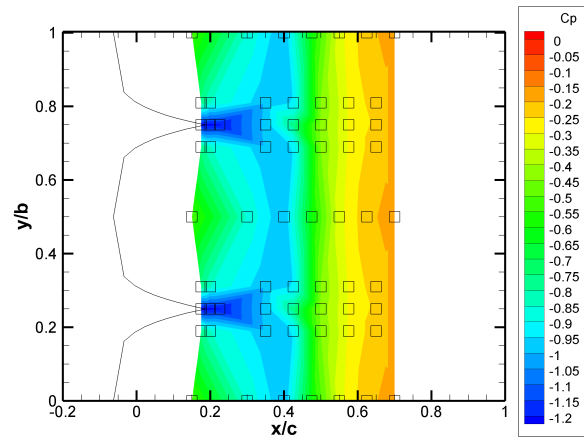


Figure 5.9: Experimental C_p contour of the power $n = 0.20$ leading edge wing at Mach 0.825.

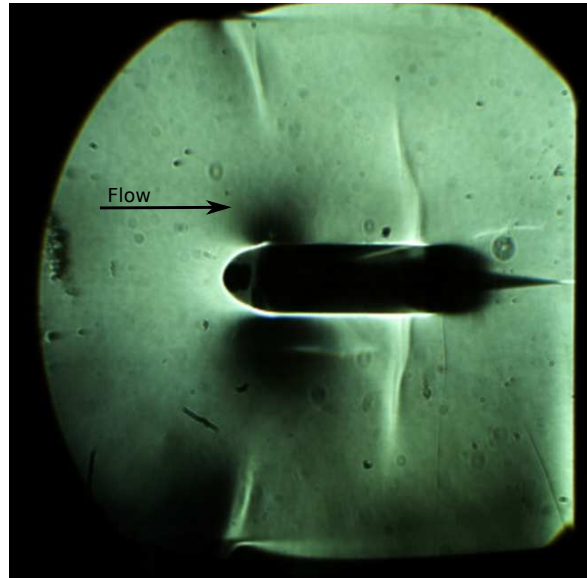
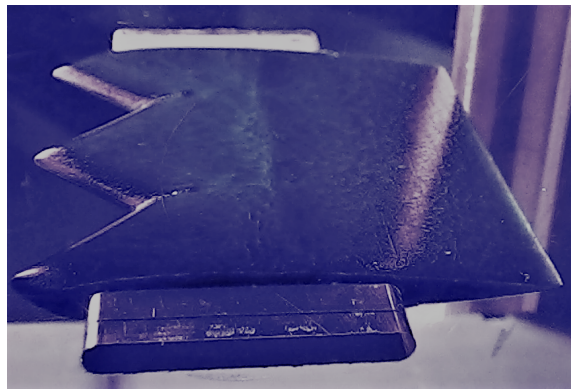


Figure 5.10: Schlieren visualization of the straight leading edge wing at Mach 0.82.

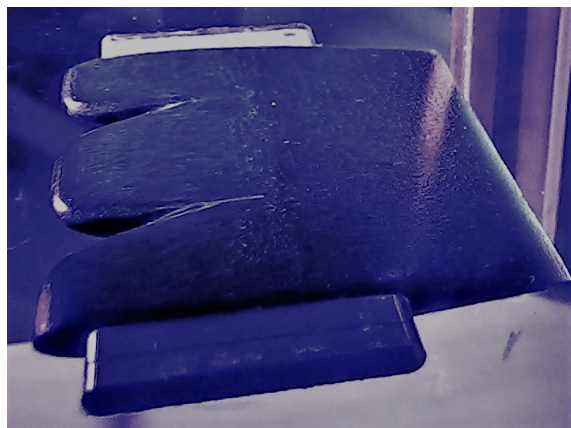
Figure 5.11 shows the surface flow pattern observed for the three wings. The flow of oil on the surface formed short streaklines and indicated the direction of flow. In addition, the accumulation of oil in certain region indicates the presence of the shockwave front, the quantity of accumulation of the oil indicates the strength of the SWBLI, and right after the shockwave the scrubbed darker area indicates that there is a separated region. By comparing the three pictures, it can be observed that the triangular and optimal wing both have a weaker shock front pattern than the straight leading edge wing. In addition, the optimal wing has a shock that is not strong enough to induce local boundary layer separation. This weaker interaction is an additional supporting argument that the optimal wing has a drag improvement.



(a) Straight leading edge



(b) Triangular



(c) Power 0.20

Figure 5.11: Surface flow visualization of three wings at Mach 0.82.

6 Conclusions and Recommendations

The goal of this research was to improve the drag characteristic of tubercled wings in transonic flow by optimizing the tubercle shape. This final chapter will provide concluding remarks, areas for improvement, and recommendations for future research on the topic.

6.1 Conclusions

The shape of triangular tubercles on a NACA 0012 profile based wing was optimized using CFD and gradient based optimization. Euler based simulation was used for the optimization and RANS was used for validation and post-optimal studies to elucidate flow behavior and investigate the differences between the original wings and optimized shape. The results from optimization and subsequent parametric study predicts that a shape modeled by a power series equation is able to reduce drag by up to 6% at zero angle of attack and at a freestream Mach number of 0.83 when compared to the straight leading edge wing. The reason for improvement is attributed to the presence of a wide peak region, a reduction of the valley region where the friction losses are the greatest, an increase in crossflow over the wing for an additional flow expansion direction, and a peaky behavior at the valley that leads to a lower Mach number before the shockwave. The performance gain of the optimal tubercled wing was verified experimentally with force measurements by a load cell, and certain flow features such as the peaky behavior was verified with pressure measurements. This study shows that the shape of tubercles can have a large impact on the performance of a wing and their design has to be taken into consideration for potential applications.

6.2 Recommendations for Future Developments

A number of potential areas for further development are identified, and they could improve the optimization process and understanding of the implication of tubercles in transonic flow. A better optimization setup could be implemented in order to better automatically explore the design space while keeping the same average chord. This could be done by applying bounds and constraints such as finding a way to constrain the planform area directly. Additionally, it is recommended to consider more starting geometries for the optimization given that gradient optimizers are a local type of optimization that depends on the initial design. Regarding the optimization algorithm, gradient free optimizers were not initially considered and are a possibility to search more globally the design space. Once the optimization process is improved, it could be of interest to optimize using RANS given enough time and computational resources.

It should also be considered to investigate the shape of the entire wing. The constant airfoil profile tubercled wings, as shown in Section 3.8, were not considered for the optimization process but could be an avenue to further explore the design space. It could additionally be of interest to look into combining tubercles with different types of airfoil profiles. The airfoil profile could also vary spanwise to locally improve wing characteristics.

Aerodynamic efficiency is an important factor in practical aerodynamics but the angle of attack of zero degrees was used for the early stages to gather a foundation of knowledge for tubercles in transonic flow, and the performance and optimization considering a lift target at an angle of attack is left as a future question, although the performance was preliminarily investigated in Section 4.6.1.

In terms of experiments, now that trends were demonstrated experimentally with some confidence, characterizing in detail the drag divergence curves and drag changes at multiple velocities should be done using a more accurate load cell or a load cell more appropriate to dynamic loadings (for example the piezo-electric load cell). It is also recommended to redesign the test section in order to limit the interactions between the test section walls and the wing. Schlieren visualization should be done with optical glass for the side windows of the test section in order to capture the full interaction between the shockwave and the wing.

Bibliography

- [1] J. Reneaux. Overview on drag reduction technologies for civil transport aircraft. In *European Congress on Computational Methods in Applied Sciences and Engineering (ECCOMAS)*, 2004.
- [2] D.M. Bushnell. Shock wave drag reduction. *Annu. Rev. Fluid Mech.*, 36:81–96, 2004.
- [3] C. van Dam. Aircraft design and the importance of drag prediction. *CFD-Based Aircraft Drag Prediction and Reduction*, 2:1–37, 2003.
- [4] R. Vos and S. Farokhi. *Introduction to Transonic Aerodynamics*, volume 110. Springer, 2015.
- [5] D. Küchemann. *The Aerodynamic Design of Aircraft*. AIAA education series. American Institute of Aeronautics & Astronautics, 2012.
- [6] A. Asghar, R.E. Perez, and M. Ferchichi. Effect of leading edge tubercles on transonic performance of airfoils. In *35th AIAA Applied Aerodynamics Conference*, page 3402, 2017.
- [7] A. Asghar, R.E. Perez, and M. Ferchichi. Transonic performance of airfoils using leading edge tubercles. In *53rd 3AF International Conference in Applied Aerodynamics*, 2018.
- [8] R.E. Perez and A. Asghar. Numerical study of the effects of leading edge tubercles on transonic performance of airfoils. In *2018 Applied Aerodynamics Conference*, page 3955, 2018.
- [9] G.B. Filho, A.L. Da Costa, A.A. de Paula, and G.R. De Lima. A numerical investigation of the wavy leading edge phenomena at transonic regime. In *2018 AIAA Aerospace Sciences Meeting*, page 0317, 2018.
- [10] V.A. Sepetauskas, B. Massucatto, A.A. de Paula, and R.G. da Silva. Wavy leading edge phenomena on transonic flow regime. In *2018 Flow Control Conference*, page 4254, 2018.

-
- [11] D.S. Miklosovic, M.M. Murray, L.E. Howle, and F.E. Fish. Leading-edge tubercles delay stall on humpback whale flippers. *Physics of Fluids*, 16(5):L39–L42, May 2004.
- [12] K.L. Hansen. *Effect of Leading Edge Tubercles on Airfoil Performance*. PhD thesis, The University of Adelaide, July 2012.
- [13] F.E. Fish and J.M. Battle. Hydrodynamic design of the humpback whale flipper. *Journal of Morphology*, 225(1):51–60, November 1995.
- [14] S. Leatherwood. *Whales, dolphins, and porpoises of the eastern North Pacific and adjacent Arctic waters: a guide to their identification*. Courier Corporation, 1988.
- [15] R.K. Edel and H.E. Winn. Observations on underwater locomotion and flipper movement of the humpback whale megaptera novaeangliae. *Marine Biology*, 48(3):279–287, 1978.
- [16] C.M. Jurasz and V.P. Jurasz. Feeding modes of the humpback whale, megaptera novaeangliae, in Southeast Alaska. *Sci. Rep. Whales Res. Inst.*, 31:69–83, 1979.
- [17] J.H.W. Hain, G.R. Carter, S.D. Kraus, C.A. Mayo, and H.E. Winni. Feeding behavior of the humpback whale, megaptera novaeangliae, in the western North Atlantic. *Fishery Bulletin*, 80(2):259–268, 1982.
- [18] H. Johari, C. Henoeh, D. Custodio, and A. Levshin. Effects of leading-edge protuberances on airfoil performance. *AIAA Journal*, 45:2634–2642, 2007.
- [19] D.S. Miklosovic, M.M. Murray, and L.E. Howle. Experimental evaluation of sinusoidal leading edges. *Journal of Aircraft*, 44(4):1404–1407, 2007.
- [20] K.L. Hansen, R.M. Kelso, and B.B. Dally. Performance variations of leading-edge tubercles for distinct airfoil profiles. *AIAA Journal*, 49:185–194, 2011.
- [21] P. Watts and F.E. Fish. The influence of passive, leading edge tubercles on wing performance. In *Proceedings of the Twelfth International Symposium on Unmanned Untethered Submersible Technology (UUST01)*, Autonomous Undersea Systems Inst., Lee, NH, August 2001.
- [22] H.T.C. Pedro and M.H. Kobayashi. Numerical study of stall delay on humpback whale flippers. In *46th AIAA Aerospace Sciences Meeting and Exhibit*, number AIAA 2008-0584, Reno, NV, 7-10 January 2008.
- [23] E.A. van Nierop, S. Alben, and M.P. Brenner. How bumps on whale flippers delay stall: an aerodynamic model. *Physical Review Letters*, 100(054502):1–4, February 2008.

-
- [24] P.W. Weber, L.E. Howle, M.M. Murray, and D.S. Miklosovic. Computational evaluation of the performance of lifting surfaces with leading-edge protuberances. *AIAA Journal of Aircraft*, 48(2):591–600, 2011.
- [25] M.W. Lohry, L. Martinelli, and J.S. Kollasch. Genetic algorithm optimization of periodic wing protuberances for stall mitigation. In *31st AIAA Applied Aerodynamics Conference*, number AIAA 2013-2905, San Diego, CA, June 24-27 2013.
- [26] S.M.A. Aftab, N.A. Razak, A.S.M. Rafie, and K.A. Ahmad. Mimicking the humpback whale: An aerodynamic perspective. *Progress in Aerospace Sciences*, 84:48–69, 2016.
- [27] K.L. Hansen, R.M. Kelso, and C.J. Doolan. Reduction of flow induced tonal noise through leading edge tubercle modifications. In *16th AIAA/CEAS Aeroacoustics Conference*, number AIAA 2010-3700, 2010.
- [28] A. Asghar, R.E. Perez, and W.D. Allan. Further parametric investigation of leading edge tubercles on the propeller performance. In *AIAA Scitech 2019 Forum*, page 0850, 2019.
- [29] J. Borg. *The Effect of Leading Edge Serrations on Dynamic Stall*. PhD thesis, University of Southampton, 2012.
- [30] C. Cai, Z. Zuo, S. Liu, F. Wu, and F. Wang. Numerical evaluation of the effect of leading-edge protuberances on the static and dynamic stall characteristics of an airfoil. In *6th International Conference on Pumps and Fans with Compressors and Wind Turbines, Institute of Physics (IOP): Materials Science and Engineering*, volume 52, pages 1–7, 2013.
- [31] A. Asghar, R.E. Perez, and W. Allan. Application of leading edge tubercles to enhance propeller performance. In *2018 Applied Aerodynamics Conference*, page 3647, 2018.
- [32] A. Gupta, A. Alsultan, R.S. Amano, S. Kumar, and A.D. Welsh. Design and analysis of wind turbine blades: Winglet, tubercle, and slotted. In *ASME Turbo Expo 2013: Turbine Technical Conference and Exposition*, pages V008T44A024–V008T44A024. American Society of Mechanical Engineers, 2013.
- [33] G.-Y. Huang, Y.C. Shiah, C.-J. Bai, and W.T. Chong. Experimental study of the protuberance effect on the blade performance of a small horizontal axis wind turbine. *Journal of Wind Engineering and Industrial Aerodynamics*, 147:202–211, 2015.
- [34] G. Abate and D.N. Mavris. CFD analysis of leading edge tubercle effects on wind turbine performance. In *15th International Energy Conversion Engineering Conference*, page 4626, 2017.

-
- [35] Z. Wang and M. Zhuang. Leading-edge serrations for performance improvement on a vertical-axis wind turbine at low tip-speed-ratios. *Applied Energy*, 2017.
- [36] C.J. Bai, Y.Y. Lin, S.Y. Lin, and W.C. Wang. Computational fluid dynamics analysis of the vertical axis wind turbine blade with tubercle leading edge. *Journal of Renewable and Sustainable Energy*, 7, 2015.
- [37] P.W. Weber, L.E. Howe, and M.M. Murray. Lift, drag and cavitation onset on rudders with leading edge tubercles. *Marine Technology*, 47(1):27–36, January 2010.
- [38] I.H. Ibrahim and T.H. New. A numerical study on the effects of leading-edge modifications upon propeller flow characteristics. In *Ninth International Symposium on Turbulence and Shear Flow Phenomena (TSFP-9)(accepted)*, 2015.
- [39] W. Shi, M. Atlar, and R. Norman. Detailed flow measurement of the field around tidal turbines with and without biomimetic leading-edge tubercles. *Renewable Energy*, 111:688–707, 2017.
- [40] W. Shi, M. Atlar, R. Norman, B. Aktas, and S. Turkmen. Numerical optimization and experimental validation for a tidal turbine blade with leading-edge tubercles. *Renewable energy*, 96:42–55, 2016.
- [41] M.D. Bolzon, R.M. Kelso, and M. Arjomandi. Tubercles and their applications. *Journal of Aerospace Engineering*, 29:1–10, 2015.
- [42] W.F. Phillips. *Mechanics of flight*. John Wiley & Sons, 2004.
- [43] W.J. McCroskey. A critical assessment of wind tunnel results for the NACA 0012 airfoil. Technical report, NASA Ames Research center, 1987. NASA Technical Memorandum 110446.
- [44] F. Palacios, J. Alonso, K. Duraisamy, M. Colonno, J. Hicken, A. Aranake, A. Campos, S. Copeland, T. Economon, A. Lonkar, et al. Stanford University Unstructured (SU2): An open-source integrated computational environment for multi-physics simulation and design. In *51st AIAA Aerospace Sciences Meeting including the New Horizons Forum and Aerospace Exposition*, page 287, 2013.
- [45] F.R. Menter. Two-equation eddy-viscosity turbulence models for engineering applications. *AIAA journal*, 32(8):1598–1605, 1994.
- [46] J. Blazek. *Computational Fluid Dynamics: Principles and Applications*. Elsevier, 2005.

-
- [47] J.E. Bardina, P.G. Huang, and T.J. Coakley. Turbulence modeling validation, testing, and development. *NASA Technical Memorandum 110446*, 1997.
- [48] Philip L Roe. Approximate Riemann solvers, parameter vectors, and difference schemes. *Journal of computational physics*, 43(2):357–372, 1981.
- [49] M. Uygun and K. Kirkkölprü. Numerical solution of the Euler equations by finite volume methods: central versus upwind schemes. *Journal of Aeronautics and Space Technologies*, 2(1):47–55, 2005.
- [50] C.D. Harris. Two-dimensional aerodynamic characteristics of the NACA 0012 airfoil in the Langley 8 foot transonic pressure tunnel. *NASA Technical Memorandum 81927*, 1981.
- [51] K.W. Noonan and G.J. Bingham. Aerodynamic characteristics of three helicopter rotor airfoil sections at Reynolds numbers from model scale to full scale at Mach numbers from 0.35 to 0.90. Technical report, NASA Langley Research Center, 1980. NASA Technical Paper 1701.
- [52] P.M. Sforza. *Commercial airplane design principles*. Elsevier, 2014.
- [53] J. Anderson. *Fundamentals of Aerodynamics*. McGraw-Hill Education, 2010.
- [54] J. Samareh. Aerodynamic shape optimization based on free-form deformation. In *10th AIAA/ISSMO multidisciplinary analysis and optimization conference*, page 4630, 2004.
- [55] C.A. Mader, J.R. RA Martins, J.J. Alonso, and E.V. Der Weide. ADjoint: An approach for the rapid development of discrete adjoint solvers. *AIAA journal*, 46(4):863–873, 2008.
- [56] R.E. Perez, P.W. Jansen, and Joaquim R.R.A. Martins. pyopt: a python-based object-oriented framework for nonlinear constrained optimization. *Structural and Multidisciplinary Optimization*, 45(1):101–118, 2012.
- [57] P.E. Gill, W. Murray, and M.A. Saunders. SNOPT: An SQP algorithm for large-scale constrained optimization. *SIAM review*, 47(1):99–131, 2005.
- [58] J. Sun and S. Hansen. Transonic nose wave drag of axisymmetric bodies. In *20th Aerospace Sciences Meeting*, page 308, 1982.
- [59] G.A. Crowell Sr. The descriptive geometry of nose cones. URL: <http://www.myweb.cableone.net/cjcrowell/NCEQN2.doc> (accessed August 2019), 1996.
- [60] H. Babinsky and J.K. Harvey. *Shock Wave-Boundary-Layer Interactions*, volume 32. Cambridge University Press, 2011.

- [61] J.E.A. John and T.G. Keith. *Gas Dynamics*. Pearson Prentice Hall, 2006.
- [62] A. Bajo and N. Simaan. Hybrid motion/force control of multi-backbone continuum robots. *The International journal of robotics research*, 35(4):422–434, 2016.

Appendices

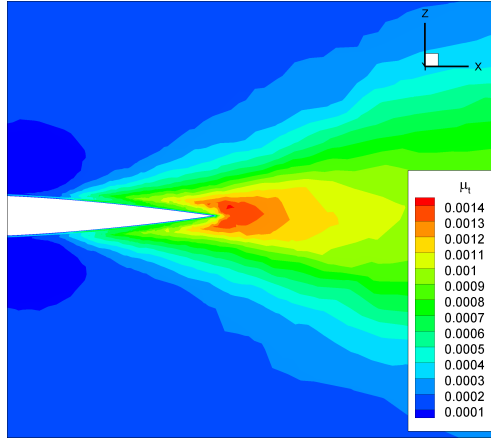
A Additional CFD Results

A.1 Turbulent Kinetic Energy and Turbulent Viscosity

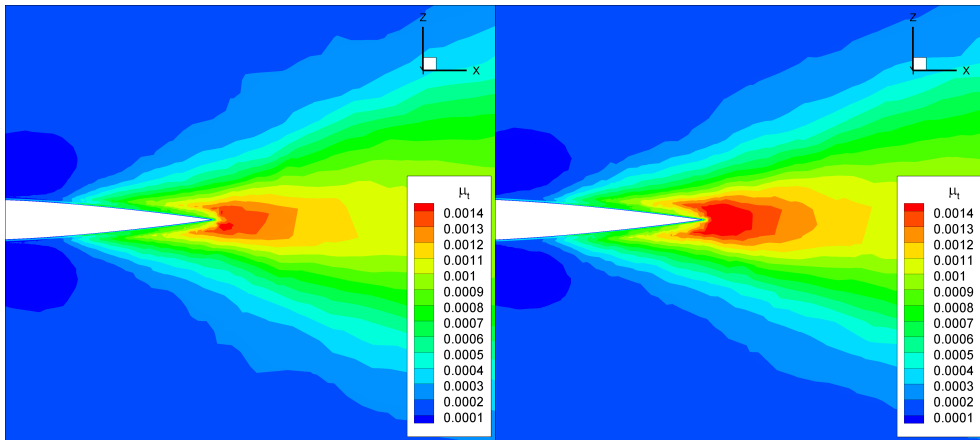
The flow downstream of the shockwave of the baseline wings was further analyzed by visualizing the turbulent viscosity which is a measure of the turbulence due to perturbations in the flow and can be a measure of losses. The turbulent viscosity at the trailing edge of the baseline wings are shown in Figure A.1 in which a contour slice is shown for both the peaks and valleys. For the triangular tubercled wing the magnitude of turbulent viscosity depends on the spanwise position. Higher values of turbulent viscosity are found after the trailing edge of the valley whereas it is very similar to the straight leading edge after the peak. For the sinusoidal leading edge wing the turbulent viscosity does not seem to change considerably spanwise and is overall of a greater magnitude than the straight leading edge wing.

The turbulent viscosity at the trailing edge of the straight leading edge wing and aligned with the peak and valley of the power $n = 0.20$ wing can be seen in Figure A.2. For the optimized wing the findings are very similar to the ones found in Perez and Asghar [8] for the triangular tubercle wing, though the optimized shape maximizes the region of lower turbulent viscosity with a wider peak and minimizes the higher turbulent viscosity region by minimizing the valley region. This turbulent viscosity variation can also be visualized with the iso-surface shown in Figure A.2d. This turbulent viscosity variation is also reflected in the variation of TKE as shown in Figures A.3, A.4 and A.5.

A.1. Turbulent Kinetic Energy and Turbulent Viscosity

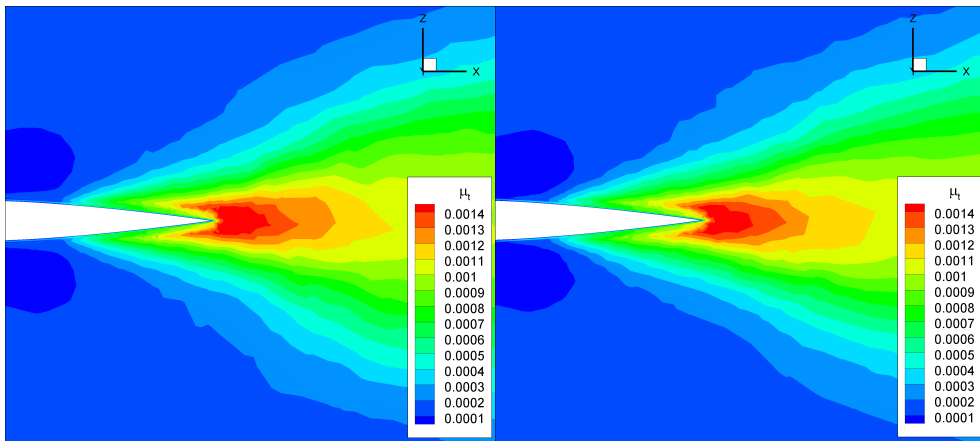


(a) Straight leading edge wing



(b) Triangular tubercle peak

(c) Triangular tubercle valley



(d) Sinusoidal tubercle peak

(e) Sinusoidal tubercle valley

Figure A.1: Turbulent viscosity for the baseline wings at Mach 0.83.

A.1. Turbulent Kinetic Energy and Turbulent Viscosity

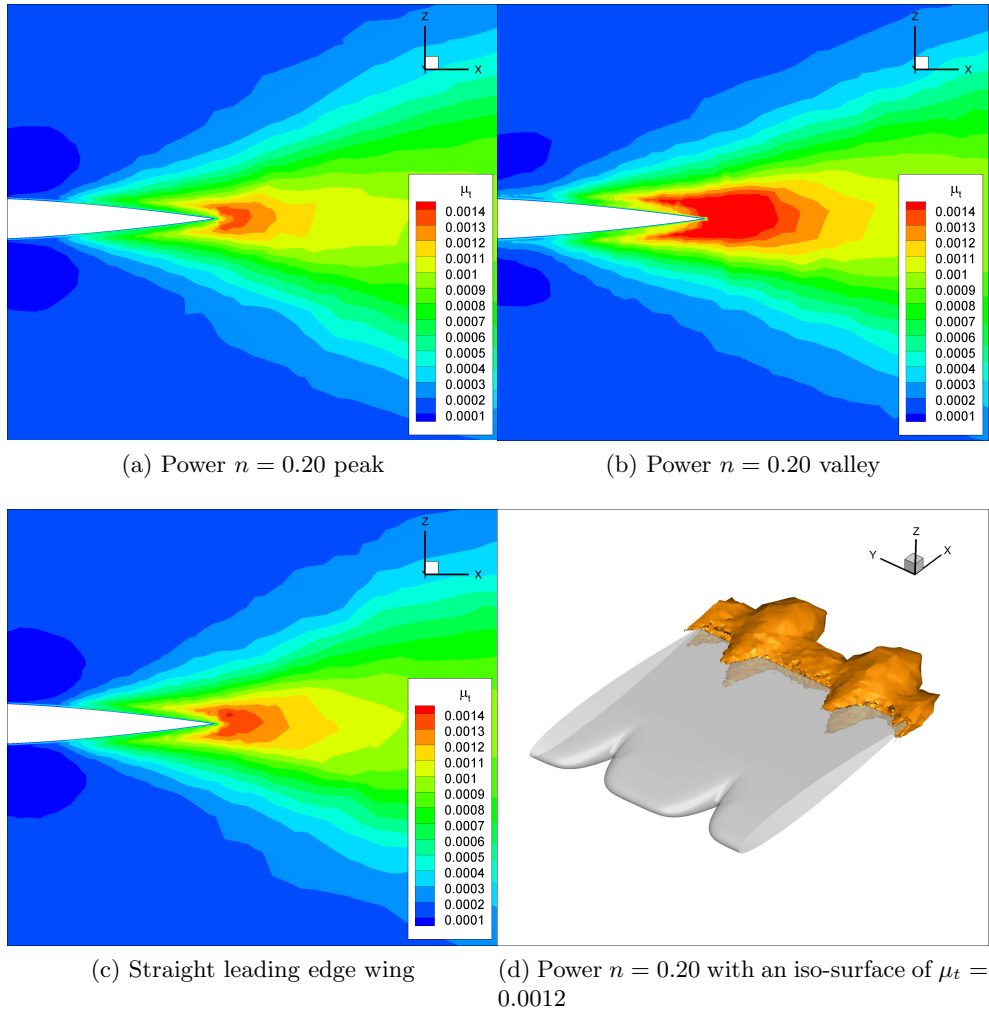
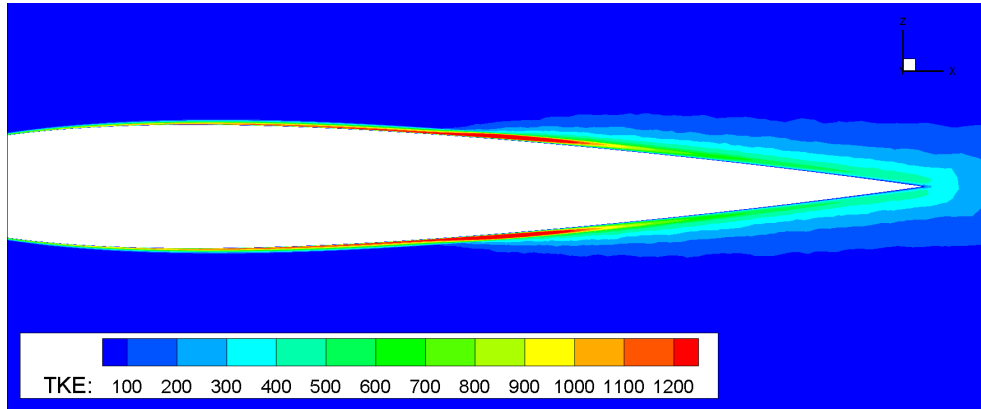
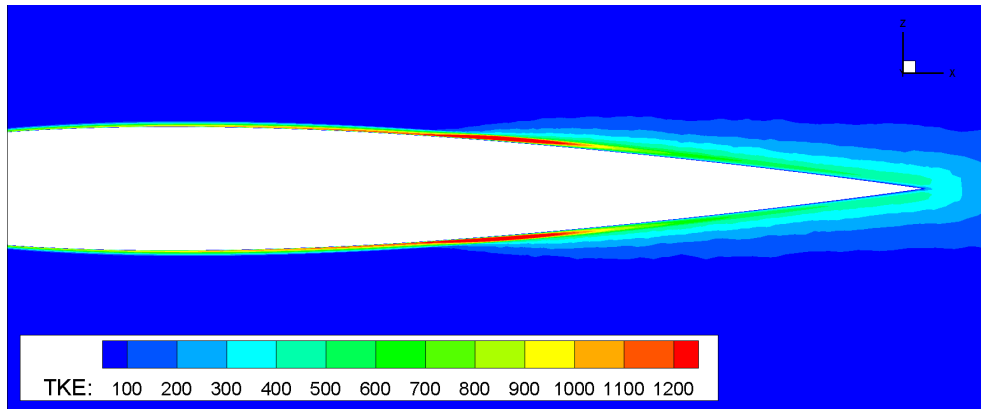


Figure A.2: Turbulent viscosity of the power $n = 0.20$ and straight leading edge wing at Mach 0.83.

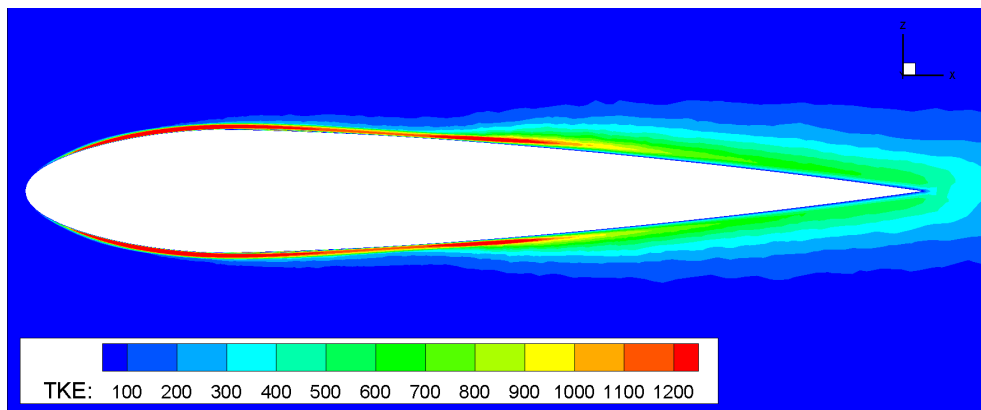
A.1. Turbulent Kinetic Energy and Turbulent Viscosity



(a) Straight leading edge wing

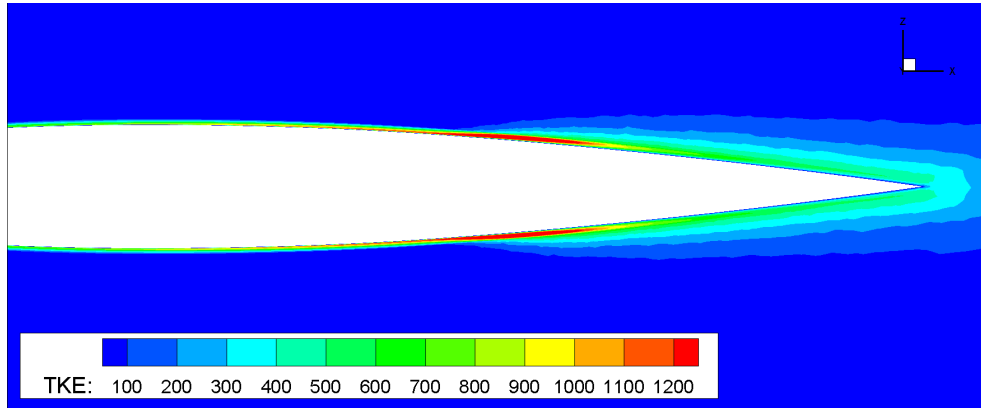


(b) Power $n = 0.20$ peak

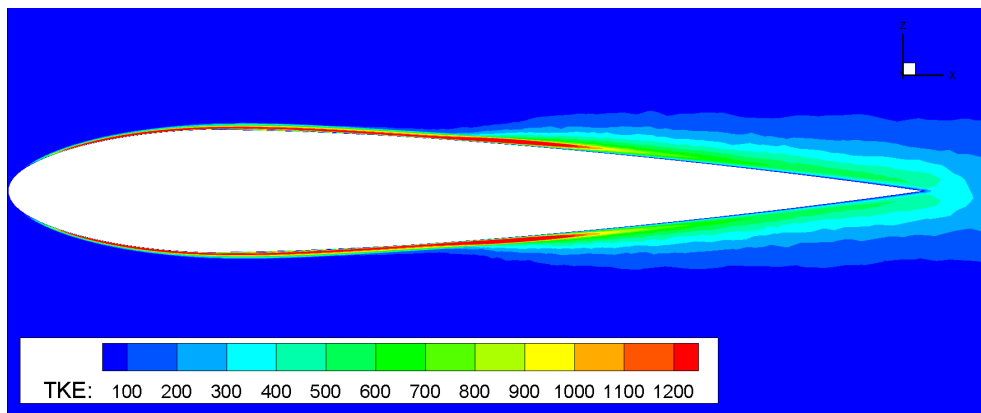


(c) Power $n = 0.20$ valley

Figure A.3: Turbulent kinetic energy for two wings at Mach 0.83.

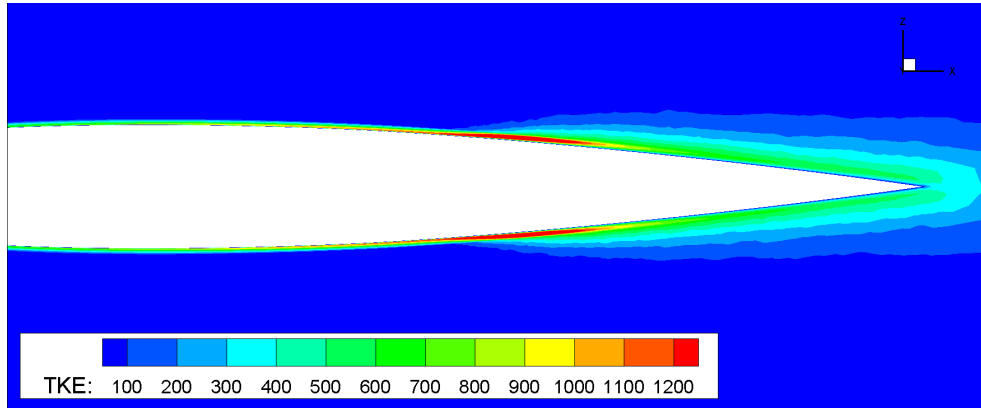


(a) Triangular tubercle peak

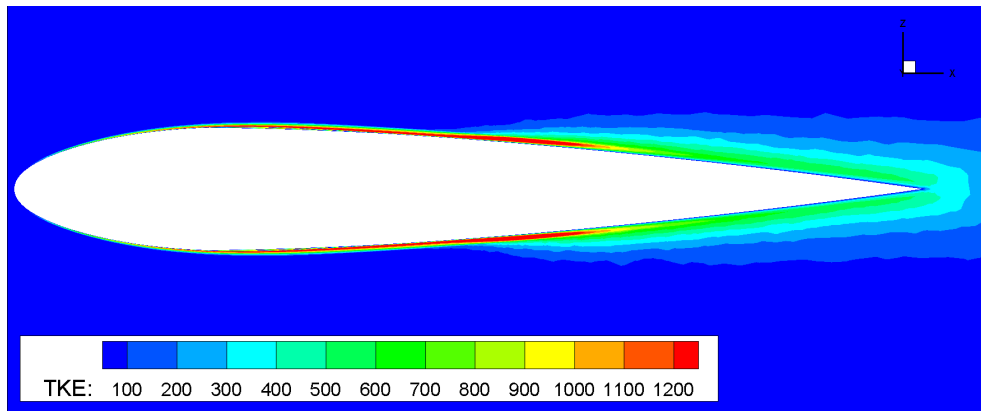


(b) Triangular tubercle valley

Figure A.4: Turbulent kinetic energy for the triangular tubercle wing at Mach 0.83.



(a) Sinusoidal tubercle peak



(b) Sinusoidal tubercle valley

Figure A.5: Turbulent kinetic energy for the sinusoidal tubercle wing at Mach 0.83.

B Additional Experiments

B.1 Compilation of Drag Measurements

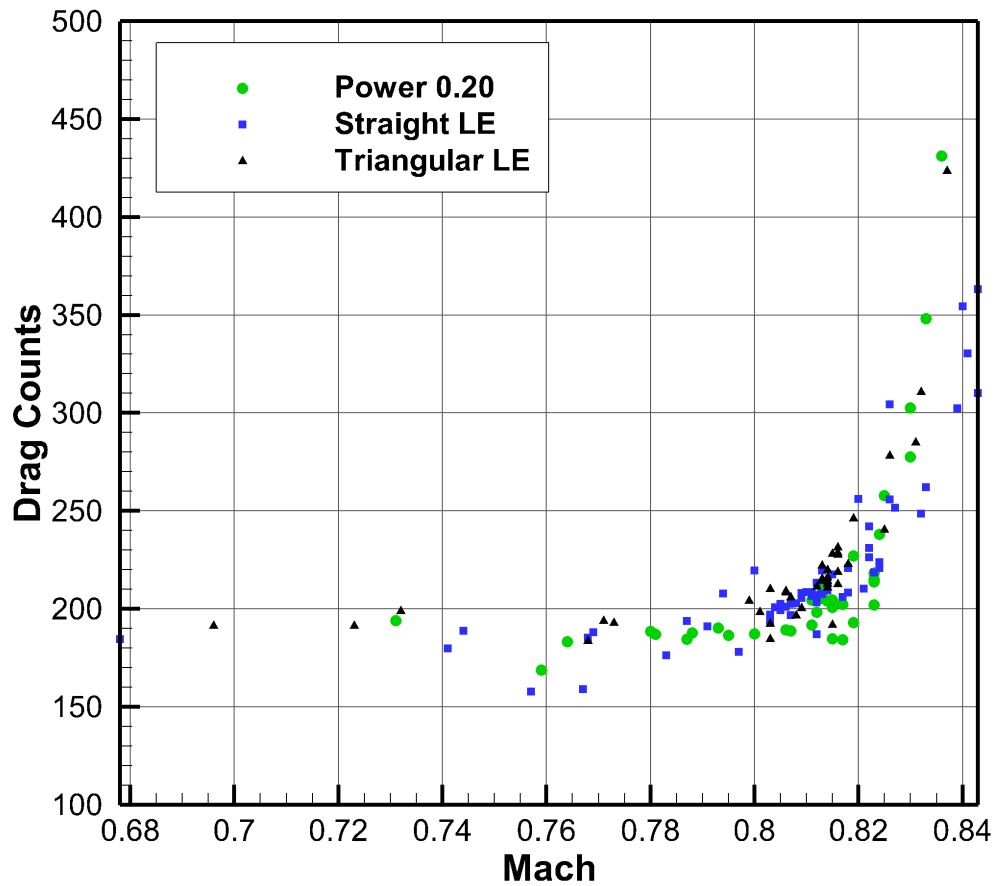


Figure B.1: Compilation of drag measurements showing the drag rise of three wings.

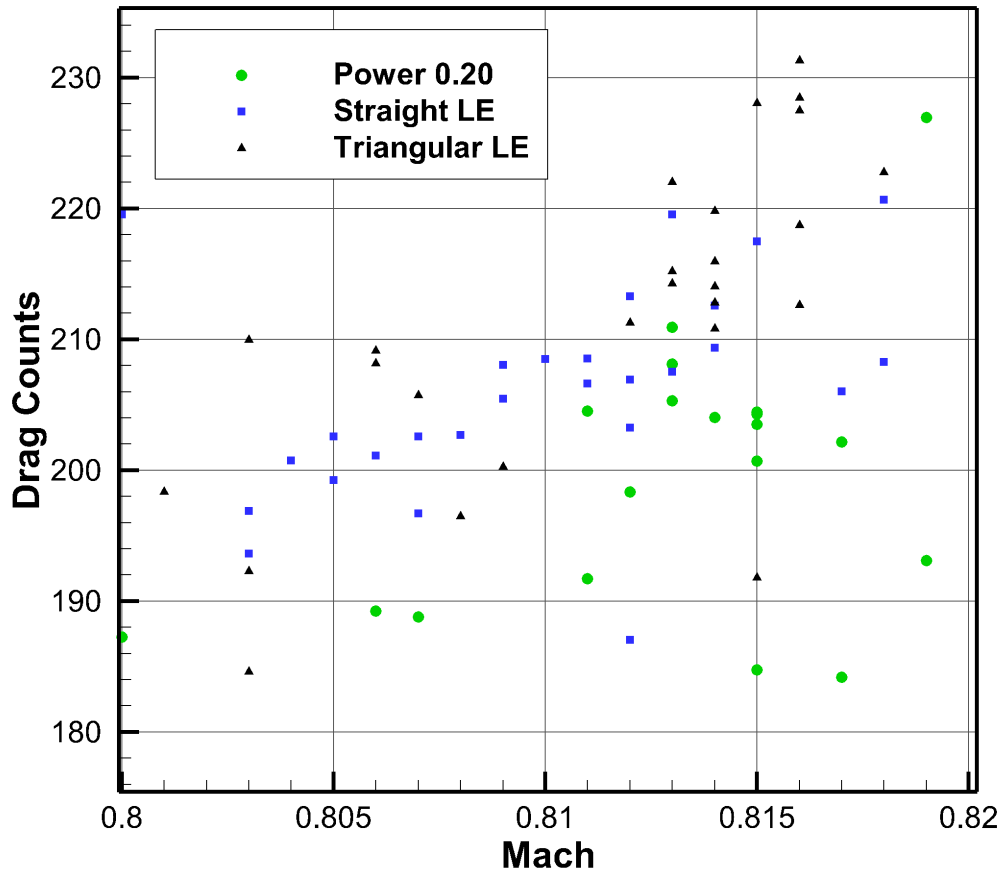


Figure B.2: Compilation of drag measurements near a Mach number of 0.81.

B.2 Schlieren Visualization

To get qualitative information of the flow, the shock flow patterns in transonic flow was recorded using a schlieren system equipped with a high speed camera as shown in Figure B.3. This was done over three models, a straight, triangular and elliptical (with an amplitude of $0.25c$ and wavelength of $0.3c$) leading edge wing. A sample of the visualization of each wing is shown in Figures B.4, B.5 and B.6.

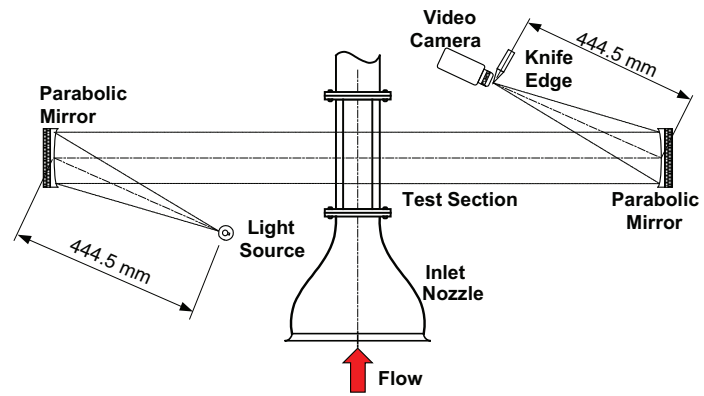


Figure B.3: Schlieren setup schematic [7].

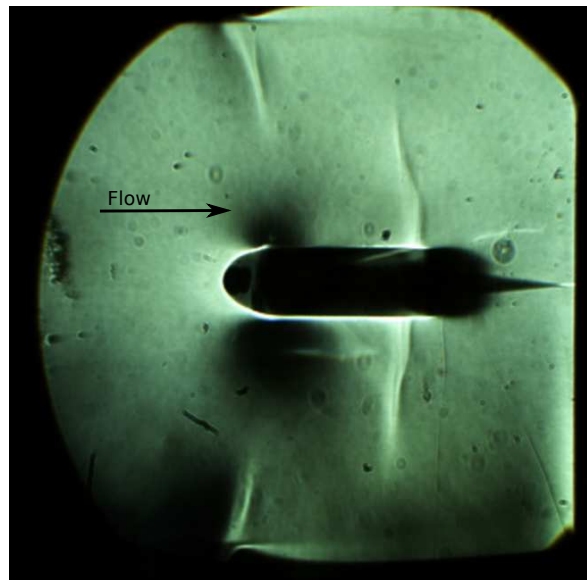


Figure B.4: Schlieren visualization of the straight leading edge wing at Mach 0.82.

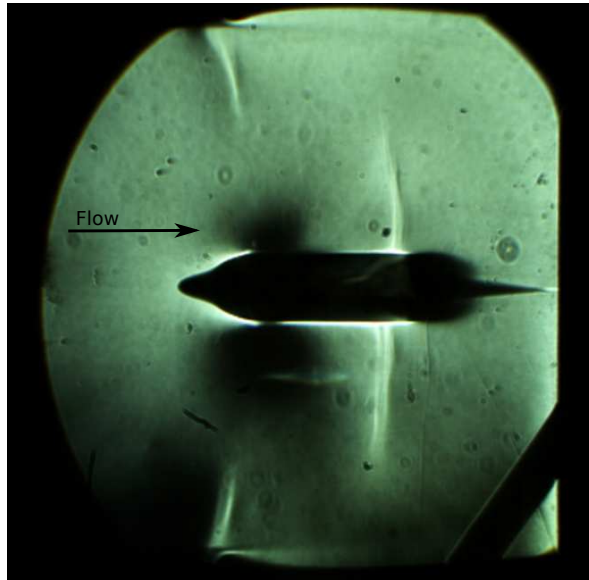


Figure B.5: Schlieren visualization of the triangular leading edge wing at Mach 0.82.

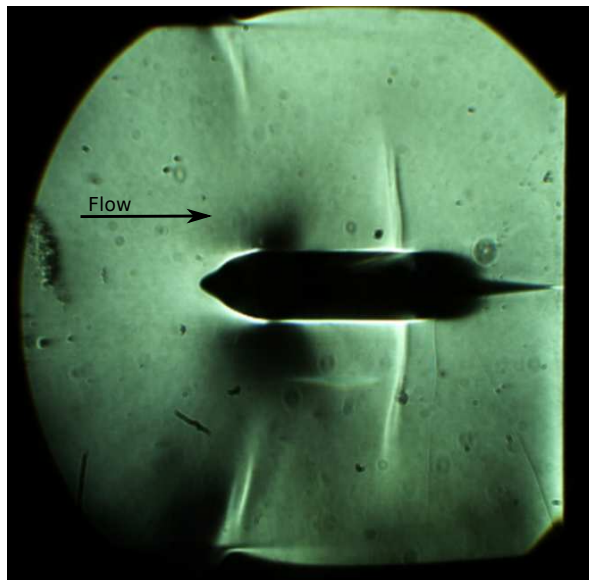


Figure B.6: Schlieren visualization of an elliptical leading edge wing (with an amplitude of $0.25c$ and wavelength of $0.3c$) at Mach 0.82.